Near-field wind mixing and implications on parameterization from float observations

Ryuichiro Inoue and Satoshi Osafune

Research Institute for Global Change, Japan Agency for Marine-Earth Science and Technology (JAMSTEC), 2-15 Natsushima-cho, Yokosuka 237-0061, Japan

Corresponding author address: Ryuichiro Inoue, Research Institute for Global Change, Japan Agency for Marine-Earth Science and Technology (JAMSTEC), 2-15 Natsushima-cho, Yokosuka 237-0061, Japan

E-mail: rinoue@jamstec.go.jp

Phone: +81-46-867-9834, Fax: +81-46-867-9835

Early Online Release: This preliminary version has been accepted for publication in *Journal of the Physical Oceanography*, may be fully cited, and has been assigned DOI 10.1175/JPO-D-20-0281.1. The final typeset copyedited article will replace the EOR at the above DOI when it is published.

Abstract

A part of near-inertial wind energies dissipates locally below the surface mixed layer. Here, their role in the climate system is studied by adopting near-inertial near-field wind-mixing parameterization to a coarse-forward ocean general circulation model. After confirming a problem of the parameterization in the equatorial region, we investigate effects of near-field wind mixing due to storm track activities in the North Pacific. We found that, in the center of the Pacific Decadal Oscillation (PDO) around 170^{o}W in the mid latitude, near-field wind mixing transfers the PDO signal into deeper layers. Since the results suggest that near-field wind mixing is important in the climate system, we also compared the parameterization with velocity observations by a float in the North Pacific. The float observed abrupt and local propagation of near-inertial internal waves and shear instabilities in the main thermocline along the Kuroshio Extension for 460 km. Vertical diffusivities inferred from the parameterization do not reproduce the enhanced diffusivities in the deeper layer inferred from the float. Wave-ray tracing indicates that wave trapping near the Kuroshio front is responsible for the elevated diffusivities. Therefore, enhanced mixing due to trapping should be included in the parameterization.

Accepted for publication in *Journal of Physical Oceanography*. DOI 10.1175/JPO-D-20-0281.1.

1. Introduction

Mid-latitude atmospheric storms can efficiently generate inertial oscillations in the surface mixed layer (ML) of the ocean. After oscillations are generated, a part of the energy in the ML radiates to the ocean interior as low-mode near-inertial internal waves (Gill 1984; D'Asaro et al. 1995). It has been hypothesized that the radiation, propagation, and breaking of near-inertial internal waves are important in maintaining stratification in the abyssal ocean (Munk 1966; Munk and Wunsch 1998).

By applying the slab ML model (Pollard and Millard 1970; D'Asaro 1985) to the global ocean, the estimated global inertial energy flux into the surface ML (hereinafter called the wind power input) is around 0.5 TW (Alford 2001; Watanabe and Hibiya 2002; Alford 2003; Watanabe et al. 2005). In addition, wind power input exhibits seasonal variability related to mid-latitude storm activities. Mid-latitude storms, whose paths are called storm tracks, display variabilities on time scales longer than the seasonal variation. For example, in the North Pacific, storm tracks develop in autumn and winter. They are affected by the position and strength of the Aleutian low, which shows a temporal variability (e.g., Sugimoto and Hanawa 2009; Di Lorenzo et al. 2015). Sugimoto and Hanawa (2009) suggested that the zonal shift of the Aleutian low on a decadal or longer time scale is associated with the Pacific–North American teleconnection pattern and the meridional shift with the west Pacific teleconnection pattern. Inoue et al. (2017) applied empirical orthogonal function (EOF) analysis to a time series of the wind energy inputs estimated by the slab model. They showed that the long-time scale variability of the near-inertial motions is also related to the Aleutian low.

Deep ocean current meter moorings also found a seasonal cycle of near-inertial internal

Accepted for publication in *Journal of Physical Oceanography*. DOI 10.1175/JPO-D-20-0281.1.

wave activities (Alford and Whitmont 2007). Similarly, the vertical diffusivities inferred from the global Argo float array, which use vertical density profiles, indicate a seasonal cycle, where the internal wave fields are enhanced in the wintertime (Whalen et al. 2012). However, only a small fraction (less than 25%) of the near-inertial energy in the ML propagates into the main thermocline (Furuichi et al. 2008, Alford et al. 2012, Rimac et al. 2016) because most of the energies dissipate in the ML. It is suggested that only low mode inertial waves can propagate into the ocean interior, and internal waves with a higher vertical mode are dissipated in the upper ocean due to the higher vertical shear and slower propagation speed (Alford et al. 2016).

In the past few decades, the role of wind energies on abyssal mixing has been investigated. Wind energies are not considered an important factor for driving abyssal mixing because internal-wave energies, which reach the main thermocline, are smaller than those caused by tides. On the other hand, the role of the near-inertial energy, which dissipates locally and immediately in the upper ocean (e.g., inside and just below the surface ML) on the climate system is less understood. It is important for mixed layer and subsurface heat budgets due to enhanced entrainments and circulation changes. We also speculate that the modulation of high-mode wave energies affects the biogeochemical properties because the energies can influence the bottom of the euphotic layer. Jochum et al. (2013) introduced parameterization, which added near-field mixing effects related to the near-inertial oscillation in the ML generated by storms, and incorporated it into a coupled ocean–atmosphere model. They found that near-inertial waves influence the climate system by deepening the tropical mixed layer, and suggested that it is important to understand tropical near-inertial wave energies qualitatively to reduce uncertainties in the parameterization.

Accepted for publication in *Journal of Physical Oceanography*. DOI 10.1175/JPO-D-20-0281.1.

In this study, we adopt the parameterization developed by Jochum et al. (2013) to a coarse-forward ocean general circulation model (OGCM) equipped with a turbulence closure model (Noh 2004) and optimized through a data assimilation approach (Osafune et al. 2015) (Section 2). In Section 3, we integrate the OGCM with parameterization for 58 years, describe near-inertial motions and waves reproduced in the OGCM, and compare the results with and without parameterization. We also discuss the possible effects of near-field wind mixing due to the storm track activities in the North Pacific, which are modulated by the Aleutian low on the decadal scale. In Section 4, we evaluate the parameterization and discuss potential improvements. Specifically, we compare the vertical diffusivities inferred from the parameterization and the Electro Magnetic Autonomous Profiling Explorer (EM-APEX) float (Teledyne Webb Research, Sanford et al. 2005) measurements. Here, the EM-APEX observed an abrupt propagation of near-inertial internal waves within the North Pacific Subtropical mode water (NPSTMW) and shear instability in the layer between NPSTMW and North Pacific Intermediate Water (NPIW) in the Kuroshio Extension (KEx) area. Finally, we discuss differences between these diffusivities.

2. Methods

2.1. Parameterization of near-field wind mixing

We adopted the near-field mixing parameterization developed by Jochum et al. (2013). This parameterization is similar to that of St. Laurent et al. (2002). St. Laurent et al. (2002) focused on mixing near steep bottom topographies due to breaking of internal tides, whereas Jochum et al. (2013) modeled mixing by near-inertial motions generated in the

Accepted for publication in *Journal of Physical Oceanography*. DOI 10.1175/JPO-D-20-0281.1.

ML due to surface wind forcing. Jochum et al. parameterized vertical diffusivities below the ML as

$$k_{niw} = \varepsilon_{niw}\frac{\Gamma}{N^2} = \frac{E_i^{flux}F(z)}{\rho}\frac{\Gamma}{N^2}, \qquad (1)$$

where Γ is the mixing efficiency and assumed to be 0.2. ρ and N^2 are the density (kg m^{-3}) and buoyancy frequency squared (s^{-2}) at each grid point, respectively.

In Eq. (1), the dissipation rate of the turbulent kinetic energy is defined as $\varepsilon_{niw} = E_i^{flux}F(z)/\rho$ (W kg^{-1}), where E_i^{flux} represents the near-inertial energy flux into the ocean interior. It has the same unit as the energy density flux (Wm^{-2}) in St. Laurent et al. (2002) and is defined as

$$E_i^{flux} = \left(1 - b_{fr}\right) \times l_{fr} \times E^{flux}, \qquad (2)$$

where b_{fr} and l_{fr} are the fraction of the energy dissipated in the ML and propagating below, respectively. Here, these are set at 0.7 and 0.5, respectively (Jochum et al. 2013). These values mean that 15% of the near-inertial energy in the ML is used to generate turbulence below the ML (near field) and another 15% is radiated away as low mode internal waves. The low mode internal waves contribute to the formation of the background internal wave field as well as interior mixing (far field). E^{flux} is the near-inertial energy flux into the surface boundary layer, $\boldsymbol{\tau} \cdot \boldsymbol{U_i}$. Here, $\boldsymbol{\tau}$ is the wind stress which forces the OGCM and $\boldsymbol{U_i}$ is the surface velocity of the near-inertial current which is estimated from the time series of outputs by a bandpass filter between 0.8 and 1.2 times of the local Coriolis frequencies. In Jochum et al. (2013), it is estimated as

$$E^{flux} = \boldsymbol{\tau} \cdot \boldsymbol{U_i} \approx \alpha \left|KE_{ML}(t+1) - KE_{ML}(t)\right|/\Delta t, \qquad (3)$$

so that k_{niw} corresponds to changes in the ML. Here α is a scaling factor to adjust the

Accepted for publication in *Journal of Physical Oceanography*. DOI 10.1175/JPO-D-20-0281.1.

global annual mean of (3) to that of simulated $\boldsymbol{\tau} \cdot \boldsymbol{U_i}$ and was set to 0.05 in Jochum et al. (2013). The bulk kinetic energy of near-inertial motions in the ML, KE_{ML}, is defined as

$$KE_{ML} = 0.5 \times \int_{-h}^{0} \rho \times \left({u^i}^2 + {v^i}^2\right) dz, \qquad (4)$$

$$u^i(t+1) \approx -T/2\pi\,[v(t+1) - v(t)]/\Delta t, \qquad (5)$$

$$v^i(t+1) \approx T/2\pi\,[u(t+1) - u(t)]/\Delta t, \qquad (6)$$

where a high-frequency velocity fluctuation in the model outputs is defined as the near-inertial velocities, u^i and v^i, which are obtained by the differences in two consecutive time steps (Δt). T is the inertial period. Equations (5) and (6) should work because the OGCM works as a lowpass filter. The computational method is selected to suit the forward time integration because variables in the right-hand side of (5) and (6) are obtained in the same time step. Otherwise, a bandpass filter would be necessary to obtain near-inertial motions.

Note that Eq. (3) is also based on the bulk mixed layer energy budget (e.g., Crawford and Large 1996),

$$\frac{\partial KE_{ML}}{\partial t} = \boldsymbol{\tau} \cdot \boldsymbol{U_i} - \rho \int_{-h}^{0} \left(-\overline{uw}\frac{\partial U}{\partial z} - \overline{vw}\frac{\partial V}{\partial z}\right) dz, \qquad (7)$$

and $\alpha^* = \int \frac{\partial KE_{ML}}{\partial t} dt \Big/ \int \boldsymbol{\tau} \cdot \boldsymbol{U_i}\, dt$ (time integral over one storm event). Crawford and Large (1996) evaluated the balance of Eq. (7) within the entire water column in their one-dimensional numerical model without motion below the ML. They also used the Station Papa mooring data to show that 80% of the total near-inertial energies exist in the ML. Crawford and Large (1996) found that α^* is an asymptote from 0 to 0.5 if the wind forcing frequency is close to that of the inertial frequency. α in Eq. (3) should be $1/\alpha^*$ according to Jochum et al. (2013). Hence, α^* is simply selected from the model output

Accepted for publication in *Journal of Physical Oceanography*. DOI 10.1175/JPO-D-20-0281.1.

(Section 3.1.1) and the newly estimated $1/\alpha^*$ is used as α.

Finally, the structure function, $F(z)$ (m^{-1}), is defined with a vertical integration equal to one as

$$F(z) = \frac{e^{(z+h)/\eta}}{\eta(1 - e^{-H/\eta})}, \qquad (8)$$

where η is a length scale and H is the bottom depth, so that $E_i^{flux} F(z)/\rho$ gives the turbulent kinetic dissipation rate, ε_{niw} (Wkg^{-1}). η is set to 2000 m by Jochum et al. (2013). Here, vertical integration of Eq. (8) between $-H$ and $-h$ becomes one (e.g., $\int_{-H}^{-h} F\,dz = 1$). We approximate the scaling factor, $\eta\left(1 - e^{-H/\eta}\right)$, by η for simplicity. Note that the depth is positive upward and has negative values. Thus, ε_{niw} decreases toward the deeper layer. H and h are positive. Vertically integrating Eq. (8) between each depth and $-h$ shows that 99 % of internal waves energy dissipates at -4790, -920, and -90 m below the ML for η = 2000, 200, and 20 m, respectively (Figs. 1a–c). In addition to η = 2000 m run, η = 40 m is arbitrarily chosen so that the near-inertial energies in the ML are confined within 200 m below the ML, which mimics breaking of higher vertical mode internal waves in the upper ocean (Figs. 1d-e).

2.2. Ocean general circulation model

This study uses version 3 of the OGCM from the Geophysical Fluid Dynamics Laboratory (NOAA, USA) Modular Ocean Model (MOM3) (Pacanowski and Griffies 2000), which has been modified for a long-term data synthesis system that derives the Estimated STate of global Ocean for Climate research (ESTOC; Osafune et al. 2015). The system applies a four-dimensional variational data assimilation method based on a strong-

Accepted for publication in *Journal of Physical Oceanography*. DOI 10.1175/JPO-D-20-0281.1.

constraint formalism. It searches for the best time-trajectory fit of the OGCM to the observations by optimizing the initial conditions of the model variables and the 10-day-mean air–sea fluxes (heat fluxes, freshwater fluxes, and wind stress) compiled from six-hourly air–sea fluxes (heat, freshwater, and momentum) of the National Center for Environmental Prediction/National Center for Atmospheric Research (NCEP/NCAR) reanalysis (Kalnay et al. 1996).

The quasi-global OGCM domain covers the region between 75°S and 80°N. The horizontal resolution is 1° in both longitude and latitude, while the vertical resolution of the 45 levels varies with thicknesses from 10 m to 400 m. An additional layer is applied for the bottom boundary layer (BBL) where the BBL model is by Gnanadesikan et al. (1998). Using Green's function approach (e.g., Menemenlis et al. 2005), the parameters related to the isopycnal (Gent and McWilliams 1990) and diapycnal (Gargett 1984; Hasumi and Suginohara 1999; Tsujino et al. 2000) diffusivities and other physical parameters have been optimized to better reproduce the deep-water masses and the abyssal circulation (Toyoda et al., 2015). For the surface boundary layer, the OGCM has used the turbulence closure model developed by Noh (2004). Noh's model applies a Mellor and Yamada-type second-order closure (e.g., Mellor and Yamada 1982) but with different boundary conditions to diagnose the turbulent energy. The ML depth, h, in Eq. (7) is defined as the shallowest depth where the buoyancy frequency is largest. Note that, since the OGCM uses the closure model, we do not apply the ML velocity modification used in Jochum et al. (2013) and the subsurface parameterization, Eq. (1), is our focus.

We referred to the original ESTOC, which contains 58 years of data from 1957 to 2014 (Osafune et al. 2014) as the control run (CTL). Using the optimized initial condition and air–sea fluxes of ESTOC, we conducted two experiments. The first involved a high-

Accepted for publication in *Journal of Physical Oceanography*. DOI 10.1175/JPO-D-20-0281.1.

frequency wind run (HFW-nJ) with six-hourly wind data added. This data was obtained by subtracting the linearly interpolated ten-day mean wind data from the six-hourly NCEP/NCAR reanalysis. The second added the parameterization of Jochum et al. (2013) to the HFW-nJ, and is hereafter called HFW-J (η = 2000 m) and HFW-Jh (η = 40 m). In those HFW cases, we decreased the high-frequency wind stress in 65-70°N by a cosine function and turned it off in 70-80°N for a stability of computations. Although the six-hourly wind data was insufficient to resolve storms in higher latitudes where the local inertial period is shorter (the detailed studies on spatial and temporal resolutions of wind data are given in Rimac et al. 2013), a correction (e.g., Nagasawa et al. 2000, Watanabe and Hibiya 2002) was not applied. Finally, since we use the prescribed heat and salinity fluxes optimized by data assimilation, temperature and salinity differences induced by the parameterization represent the pure ocean response without damping at the sea surface as explained in Osafune et al. (2020).

3. OGCM

3.1. Results

3.1.1. Near-inertial motions in the ML

Here and in the next section, the near-inertial motions and waves reproduced in the OGCM are described to introduce the parameterization by Jochum et al. (2013). Figures 2a-d depict the excitation of inertial motions after a storm event at 49.5°N, 174.5°E using HFW-nJ. The near-inertial current is generated at the surface after t=285 (elapsed hour from the start, 1957/1/1). Within a few inertial periods (the inertial period is about 15.8 hours at 49.5°N), the velocity in the ML is homogenized. The near-inertial oscillation

Accepted for publication in *Journal of Physical Oceanography*. DOI 10.1175/JPO-D-20-0281.1.

propagates below the ML after t=360. A comparison between $\int \boldsymbol{\tau} \cdot \boldsymbol{U_i}\, dt$ (time integral of the OGCM's output every three hours from the beginning for one month, hereafter $\int \boldsymbol{\tau} \cdot \boldsymbol{U_i}$), time integral of E^{flux}, $\int E^{flux}\, dt$ (hereafter $\int E^{flux}$), and KE_{ML} (Fig. 2e) shows that the $\int E^{flux}$ is higher because it integrates positive values as shown in Eq. (4). The $\int \boldsymbol{\tau} \cdot \boldsymbol{U_i}$ is largest. The average ratio of two, $\overline{KE_{ML}/\int \boldsymbol{\tau} \cdot \boldsymbol{U_i}}$, while $\boldsymbol{\tau} \cdot \boldsymbol{U_i}$ is positive (energy is brought into the ocean), has a value of 0.1. Here, we assume that this condition mimics the $\alpha^* = \int \frac{\partial KE_{ML}}{\partial t} dt / \int \boldsymbol{\tau} \cdot \boldsymbol{U_i}$ over events because inertial motions dominate high-frequency motions in the ML when there is an inertial energy flux. Figure 3 shows an example of successive storm events at 31.5°N, 174.5°E. The storm continuously passed this location every 3–4 days. The wind stress due to the next storm event modulates the pre-existing current. Again, $\int E^{flux}$ is larger than KE_{ML} and $\int \boldsymbol{\tau} \cdot \boldsymbol{U_i}$ is highest. The $\overline{KE_{ML}/\int \boldsymbol{\tau} \cdot \boldsymbol{U_i}}$ with $\boldsymbol{\tau} \cdot \boldsymbol{U_i} > 0$ becomes 0.04, which is smaller than the single storm case. This is possibly because successive storms damped the pre-existing inertial currents in the ML due to the mismatch between wind and current directions.

Finally, we found that the monthly average E^{flux} estimated from the last term of Eq. (3) with $\alpha^* = 0.2$ ($\alpha = 5$) in January 1957 (Figs. 4a and c) are 2.38 TW and 0.26 TW by including and excluding the equatorial region, respectively. On the other hand, the estimated global wind energy input, $\int \boldsymbol{\tau} \cdot \boldsymbol{U_i}\, dA$, from the output of HFW-nJ every three hours in January 1957 (Figs. 4b and c) are 0.24 and 0.22 TW by including and excluding the equatorial region (5°N-5°S), respectively, which are smaller than the annual mean values in previous studies. Although a mean value of the global $\alpha^* = \overline{KE_{ML}/\int \boldsymbol{\tau} \cdot \boldsymbol{U_i}}$ estimated in $0 < KE_{ML}/\int \boldsymbol{\tau} \cdot \boldsymbol{U_i} < 0.5$ is 0.08, we use the larger α^* $(= 0.2)$ in this study because in Eq. (3) the damping of KE_{ML} is also treated as the energy input and

Accepted for publication in *Journal of Physical Oceanography*. DOI 10.1175/JPO-D-20-0281.1.

E^{flux} matches $\int \boldsymbol{\tau} \cdot \boldsymbol{U_i}\, dA$ better. Jochum et al. (2013) noted the existence of high vertical diffusivities and the importance of understanding near-inertial motions in the equator. The parameterization implicitly assumes that near-inertial motions dominate the high frequency motions in the ML, however, this assumption cannot be true for the equatorial region because the inertial period is relatively long and a frequency of non-local motions can be close to the inertial period.

3.1.2. Near-inertial internal waves

After the radiation from the ML, near-inertial motions propagate into the ocean interior as near-inertial waves. Figure 5 shows the bandpass-filtered (between Coriolis frequencies of 30 and 35°N) meridional cross-section of the meridional velocities along 174.5°E. From Fig. 3, near-inertial motions are generated in the ML before t = 259 (Figs. 5a–b). The low-mode near-inertial waves are dominant in these velocity sections (e.g., Nagasawa et al. 2000). The velocity fields indicate that the low-mode near-inertial waves originate from latitudes where the band propagates southward (Figs. 5c–d). Another storm event is present around t = 600 (Fig. 3), but it has weaker near-inertial motions in the ML due to the deeper ML. This event seems to generate low-mode waves in the latitude band (Fig. 5e). The time series of variances, where two-dimensional horizontal wavenumber spectra of the meridional velocities (without a frequency filter) were integrated in the zonal direction in 9.5–40.5°N and 143.5°E–179.5°W, also indicate the dominance of southward propagation for linear internal waves under influence of the beta effect (e.g., Gill 1984; D’Asaro et al. 1995; Nagasawa et al. 2000). Due to the beta effect, the largest variance changes should occur along the meridional wavenumber in time (Fig.

Accepted for publication in *Journal of Physical Oceanography*. DOI 10.1175/JPO-D-20-0281.1.

6). The horizontal scale of southward-propagating near-inertial waves in the meridional direction decreases with time, and waves dissipate through the viscous effect in the OGCM. Due to the low horizontal resolution (one degree) and limited vertical resolution, the OGCM cannot reproduce near-inertial waves with higher vertical modes. Since the OGCM cannot reproduce the higher vertical modes and the vertical mixing parameterization used in the OGCM is independent on the modeled vertical shear, the enhanced shear due to near-inertial currents in the ML does not increase the vertical diffusivities below the ML. Therefore, it is reasonable to introduce the parameterization by Jochum et al. (2013) in the OGCM. Note that this parametrization is not necessary if a numerical model resolves high vertical modes as well as wave-wave interactions and vertical mixing parameterization considers the effects of enhanced shears through the Richardson number.

3.1.3. Enhanced mixing below the ML: Comparison between four cases

Figure 7 shows the same ML deepening event as that in Fig. 2 (49.5°N) for the CTL and HFW-nJ cases. Figure 7(a) shows that the CTL case does not include high-frequency wind forcing and the high-shear squared layer is confined near the sea surface. The ML depth is similar in those cases because convection due to sea surface cooling causes ML deepening (Figs. 7a–b) in the wintertime but the thermocline below the ML is thicker in the HFW cases. The difference between the HFW cases is much smaller than those between the CTL and HFW cases (not shown). The vertical profiles of a monthly average (within January 1957) vertical diffusivity estimated in the OGCM show that the diffusivities increase below the ML in the HFW-J and HFW-Jh cases (Fig.7c), that mimic

Accepted for publication in *Journal of Physical Oceanography*. DOI 10.1175/JPO-D-20-0281.1.

the shear instability due to near-inertial waves (HFW-J) and breaking of higher vertical mode internal waves below the ML (HFW-Jh). Its increase occurs deeper than the ML base due to the higher stratification just below the ML. The maximum value is ~1.8×10^{-5} m^2 sec^{-1} in the HFW-Jh case.

The horizontal distributions of the differences between the yearly average (final 58th year, 2014) temperatures from the CTL and HFW-nJ cases (HFW-nJ minus CTL, Figs. 8a–d) show the effects of high-frequency wind forcing. The water is warmed, except for that in the Atlantic and Southern Ocean, and the differences are typically less than 2 °C at the surface (-5 m depth) and subsurface (-105 m depth) (Figs. 8a–b). The differences are smaller (~1 °C) in the deeper layers but there are more cooling places than in the shallower layers (Figs. 8c–d). The upper and lower layer should be cooled and warmed, respectively, if surface mixing is enhanced due to the stronger wind forcing and temperature determines stratification. The ML deepening also cannot explain warming below the ML depth. Therefore, we speculate that these changes are due to changes in circulations.

The temperature differences between the HFW cases (HFW-J minus HFW-nJ, Figs. 8e–h) show that the surface and subsurface waters are cooled (Figs. 8e–g) and it is warmed in the deeper layer (Fig. 8h) of the equator and subtropical regions, which is expected from vertical mixing in the thermally stratified water. The surface and subsurface waters show smaller scale temperature modulations around the storm track in the mid latitudes where a deeper ML is formed. The differences between the HFW cases (HFW-Jh minus HFW-nJ, Figs. 8i–l) show that the surface and subsurface waters are cooled (heated) in the western (eastern) side of the Pacific and Atlantic. Those differences are much larger than those between the CTL and HFW-nJ cases. Water is cooled in the

Accepted for publication in *Journal of Physical Oceanography*. DOI 10.1175/JPO-D-20-0281.1.

deeper layer of the North Atlantic, and mid- and low-latitudes of the Pacific and Indian Ocean (Fig. 8k-l). The horizontal distributions of k_{niw} in the HFW-Jh case show enhanced mixing at the equator (not shown) as expected in Section 3.1.1 (Fig. 4). Since the east–west contrast in the Pacific and Atlantic Oceans is appeared in other years, we speculate that vertical mixing generates the pattern through an adjustment process. Due to those uncertainties in the equatorial region, we turn off the parameterization between 20°N and 20°S to isolate the effects of the near-field wind mixing associated with the storm track in the mid latitude of the North Pacific in the next section.

3.2. Discussion

To visualize the impact of the near-field wind mixing on the climate signal, we investigate SST by focusing on the Pacific decadal oscillation (PDO), which is the dominant year-round pattern of the monthly North Pacific SST variability (e.g., Mantua et al. 1997). Using the observed SST data, which is assimilated in ESTOC, we applied empirical orthogonal function (EOF) analysis to the monthly SST anomaly from 1971 to 2014. Here, this first principal component is used as the PDO index in this study (Figs. 9a and 11a). The corresponding EOF shows the characteristic structure of the PDO: it has a negative anomaly in the western-central region, which is surrounded by a horseshoe-shaped positive anomaly (Fig. 9a).

Figures 9b–c show the regression coefficient of the monthly SST anomaly in each experiment on the PDO index. The regression pattern of the CTL is similar to the PDO pattern, indicating that the PDO is well reproduced in the CTL. Although the regression patterns are altered in the HFW cases (e.g. Fig.9c for the HFW-nJ), they retain the

Accepted for publication in *Journal of Physical Oceanography*. DOI 10.1175/JPO-D-20-0281.1.

characteristic structure of the PDO. The differences in the regression coefficients within the HFW-nJ and HFW-J (Fig. 10a), which depict the impact of the near-field wind mixing, are positive around the center of action of the PDO at 170°W in the mid latitudes that is shown as the negative spatial peak (e.g., the black box in Fig. 10a), meaning that the regression coefficient is decreased, therefore, the PDO signal is weakened at the surface.

The reason for the decreased regression coefficient is inferred from the vertical cross-section along 170°W (Figs. 10b–c) where the regression coefficient decreases in the deeper depth due to the smaller influence from the sea surface. Applying parameterization decreases (increases) the regression coefficient in the shallower (deeper) depth for both the HFW-J (Fig. 10b) and HFW-Jh (Fig. 10c), implying that water is vertically exchanged by mixing and transfers the PDO signal into the deeper layer. A comparison between the PDO index (Fig. 11a) and the time series of the monthly SST anomaly averaged over the black box (Fig. 11b) confirmed that the SST anomaly in the center of action of the PDO where the negative regression coefficient is large also corresponds to a negative correlation. The difference in SST anomalies between HFW cases (HFW-J minus HFW-nJ in Fig. 11c) is negatively correlated with the SST anomaly in the CTL, which is same for the HFW-Jh (not shown). Thus, mixing reduces the cold and warm anomalies in the positive and negative PDOI periods, respectively, consistent with the idea that it transfers the PDO signal into the deeper layer.

These results indicate that near-field wind mixing is important on the climate system, and suggest that the impact of the atmospheric forcing on the subsurface ocean can be underestimated in OGCMs if there is no near-field wind mixing. However, the accuracy of the parameterization remains unknown. In the next section, we clarify the parameterization using EM-APEX float measurements in the North Pacific.

Accepted for publication in *Journal of Physical Oceanography*. DOI 10.1175/JPO-D-20-0281.1.

4. Observations

4.1. Results

To evaluate the parameterization and discuss its possible improvement, we analyzed the results from an EM-APEX float experiment conducted in November 2015 in the KEx area by R/V Hakuho Maru (KH-15-4 cruise). The EM-APEX float is a kind of autonomous ARGO-type float equipped with electrodes to measure voltages from seawater motions in the Earth's magnetic field. The float is also equipped with CTD (conductivity, temperature, and pressure) sensors. The vertical resolutions of CTD and EM data are 3–4 and 5–6 dbar, respectively. The data are interpolated every 6 dbar. The vertical shear and density gradient are estimated by the first differentiation so that the 6 dbar scale vertical gradients are estimated to calculate the Richardson number, Ri, as

$$Ri = N^2 / \left[\left(\frac{\partial u}{\partial z} \right)^2 + \left(\frac{\partial v}{\partial z} \right)^2 \right], \qquad (9)$$

where N^2 is the buoyancy frequency squared. u and v are the zonal and meridional velocities from the float, respectively.

On November 24, 2015 at 34.0°N and 140.1°E, one EM-APEX float was deployed. The float was moved eastward along the KEx and observed a few storm events until January 15, 2016 (Fig. 12). The continuous sampling mode was applied, the samplings were acquired using up and down profiling. Each experiment acquired 594 profiles. Sampling depth was changed from 500 dbar to 1200 dbar following the vertical propagation of internal waves after a storm event. On December 10, a storm passed by the float, and the inertial oscillation was observed in the ML. At the base of the ML, the

Accepted for publication in *Journal of Physical Oceanography*. DOI 10.1175/JPO-D-20-0281.1.

shear increases and Ri drops below 0.25, indicating shear instabilities. Similar to the OGCM, the near-inertial waves begin to propagate below the ML after a few inertial periods. The waves also penetrate through the NPSTMW (150~350 dbar) because the buoyancy frequency is higher than the local Coriolis frequency, even though the stratification of NPSTMW is low. A high shear layer (not shown) where Ri is less than 0.25 is created between the NPSTMW and NPIW (600~800 dbar) after December 20. This unstable layer was observed for about 2 weeks and covered about 460 km, suggesting that near-inertial waves induce mixing in the main thermocline and dissipate both NPSTMW and NPIW after radiation from the ML along the KEx.

4.2. Discussion

4.2.1. Modification of the near-field wind mixing parameterization

The EM-APEX observations suggest that near-inertial waves reach the main thermocline in the KEx region just after radiation from the ML due to the low stratification from the NPSTMW. Here, we estimate the average turbulent kinetic energy dissipation rate, $\langle\varepsilon\rangle$, over this event using the parameterization by Kunze et al. (1990). This parameterization uses the reduced shear squared, $ReSh^2 = (\partial u/\partial z)^2 + (\partial v/\partial z)^2 - 4N^2$, in an unstable region of the shear instability (Ri<0.25), which gives

$$\langle\varepsilon\rangle = fr \cdot \Delta z^2 \frac{\langle ReSh^2 \sigma_{grw}\rangle_c}{24}, \qquad (10)$$

where fr is the fraction of samples with Ri<0.25 to obtain the average ε over the period, Δz has a vertical resolution of 6 dbar, and σ_{grw} is the growth rate of the shear instability $\sigma_{grw} = (\partial u/\partial z + \partial v/\partial z - 2N)/4$. The average vertical diffusivity from the

Accepted for publication in *Journal of Physical Oceanography*. DOI 10.1175/JPO-D-20-0281.1.

EM-APEX over the period (December 13-January 3) is defined as

$$\langle k_{EM} \rangle = \frac{\Gamma \langle \varepsilon \rangle}{\langle N^2 \rangle_c}. \qquad (11)$$

To calculate diffusivities from Eq. (1), the EM-APEX's velocity data are interpolated every 6 dbar and 6 hours and high-pass–filtered at 1 cpd. The filtered EM-APEX's velocity data are also vertically averaged over the ML to estimate KE_{ML} in Eq. (3). $\eta =$ 2000 and 40 m are used. Figure 13a compares the vertical diffusivities obtained by Eqs. (11) and (1). These two estimations show discrepancies. $\langle k_{EM} \rangle$ show higher values in the deeper layer and lower values in the low stratification layer (NPSTMW) because waves are stretched in the low stratification during vertical propagation. For $\eta =$ 2000 m, k_{niw} is inversely proportional to the stratification because the structure function, F, defined by Eq. (8) is fairly uniform compared to $\eta =$ 40 m case (Figure 13c) and k_{niw} is smaller than $\langle k_{EM} \rangle$. For $\eta =$ 40 m, k_{niw} decreases with depth which is consistent with $\langle k_{EM} \rangle$ above 300 dbar but its magnitude is overestimated. In addition, enhanced mixing is not reproduced by Eq. (1) in both $\eta =$ 2000 and 40 m cases.

It is possible that the parameterization should consider effects of the stretching of waves. Hence, we assume that F in Eq. (8) should be defined in the WKB stretched coordinate as

$$F(z_{WKB}) = \frac{e^{(z_{WKB} + h_{WKB})/\eta_{WKB}}}{\eta_{WKB}}, \qquad (12)$$

where

$$z_{WKB} = \sum_{z} \Delta z \left(\frac{N}{N_0} \right), \qquad (13)$$

and N_0 is set to 3cph. Similar to above, we set $\eta_{WKB} =$ 2000 and 40 m. In the calculation of k_{niw}, $F(z_{WKB})$ is calculated in the WKB stretched coordinate, and then

Accepted for publication in *Journal of Physical Oceanography*. DOI 10.1175/JPO-D-20-0281.1.

the OGCM's vertical coordinate, z, is converted to z_{WKB} based on Eq. (13). Both are used to estimate F at z.

Figures 13a–c compare the newly calculated k_{niw} and F with the EM-APEX $\langle k_{EM} \rangle$. For $\eta_{WKB} = 2000$ m case, there is no difference except for the depth where $N < N_0$ because the vertical change of F is small. For $\eta_{WKB} = 40$ m case, WKB stretching improves the modeled diffusivities in the upper part of NPSTMW but underestimates the diffusivities between NPSTMW and NPIW because the stratification is higher than N_0 even in the NPSTMW (Fig. 13d). Therefore, $|z_{WKB}(z)|>|z|$. Although it is possible to choose a different value of N_0 for the improvement, we hypothesize that the enhanced mixing in the deeper layer is caused by a mechanism not considered in the parameterization. In the next section, we investigate a mechanism that would efficiently bring wave energies to the deeper layer and generate shear instabilities between the NPSTMW and NPIW.

4.2.2. Possible mechanism of the internal wave breaking

In Section 4.1, we implicitly assumed that shear instabilities between NPSTMW and NPIW are generated by near-inertial waves upon applying the parameterization by Jochum et al. (2013). However, it is possible that the observed low Ri, which is an indicator of the shear instability, is created by trapping near-inertial internal waves caused by spatial changes in the vertical component of the relative vorticity or vertical shear (e.g., Kunze 1985; Whitt and Thomas 2015). In this scenario, vertical propagation is limited within the negative relative vorticity or high vertical shear areas. Consequently, the low mode internal wave energy is also trapped and used to drive vertical mixing (e.g., Lee

Accepted for publication in *Journal of Physical Oceanography*. DOI 10.1175/JPO-D-20-0281.1.

and Niiler 1998; Zhai et al. 2009). Therefore, this cannot be represented by the parameterization used in this study.

To examine the possibility of trapping, the ray path of the near-inertial waves generated in the ML near the KEx is calculated during the EM-APEX measurements. To calculate the geostrophic flow fields and relative vorticities, we use the monthly mean global ocean eddy-resolving reanalysis (1/12° horizontal resolution and 50 vertical levels, Global_ReAnalysis_phy_001_030) data from December 2015, which was provided by the Copernicus Marine Environment Monitoring Service (CMEMS) in the European Union (http://marine.copernicus.eu/). The absolute sea surface height and a trajectory of the EM-APEX float (Fig. 14a) indicate that the float moves along the south side of the Kex, which is consistent with the existence of NPSTMW in the EM-APEX float time series (Fig. 12). We chose one cross-section normal to the KEx to represent the density and velocity structures during the period when a low Ri was observed in late December. For simplicity, we assume that neither the density nor the velocity structures change along the southeastward current. The coordinate system is rotated 45° in the clockwise direction and used to solve the ray equation (Appendix A). The vertical shear estimated from the model velocities (Fig. 14b) is almost the same as that estimated from the geostrophic balance in the KEx (not shown). We use the modeled velocity to estimate the relative vorticity, ζ_g, and inverse geostrophic Richardson number, Ri_g^{-1} (Figs. 14c and d; Appendix A).

Ray tracing indicates that near-inertial internal waves freely propagate below the NPIW if ζ_g at the wave's starting point is close to 0 or positive and the waves can satisfy the trapping condition in the negative ζ_g area (Figs. 14e–f). It is known that near-inertial waves are trapped if the intrinsic frequency is equal to the minimum internal wave

Accepted for publication in *Journal of Physical Oceanography*. DOI 10.1175/JPO-D-20-0281.1.

frequency (e.g., Whitt and Thomas 2015). Note that the contribution of the vertical shear on the trapping is important near the KEx. However, the spatial change of ζ_g is more important in the south of the KEx (Fig. 14f). From ray tracing, we conclude that the shear instabilities between NPSTMW and NPIW are generated by the near-inertial wave trapping where even the low-mode wave's energy is used for mixing. Therefore, it is suggested that a new parameterization is necessary to represent near-field wind mixing near the western-boundary currents and eddies, where the fronts and the trapping of near-inertial waves containing low modes are expected.

In western boundary regions, the Antarctic Circumpolar Current and tropics, anticyclonic areas (ζ_g<0) are often found at the sea surface (Figure 15a). When ζ_g is negative at the sea surface, frequencies of near-inertial motions in the ML are decreased. Then, near-inertial waves radiated from the ML are trapped in the deeper layer where an intrinsic frequency of waves corresponds to the minimum near-inertial frequency, ω_{min} (Appendix A) as seen in the KEx. Here, it is assumed that the depth of the deepest layer, where ω_{min} normalized by the local Coriolis frequency (ω_{min}/f) is smaller than 0.95, can be regarded as the possible trapping layer (e.g. Figure 5 in Whitt and Thomas 2013). It is shown that the layer depth becomes deeper in those ζ_g<0 areas (Figure 15b). Therefore, it is suggested that a new parameterization which considers the trapping of near-inertial waves would be required in a part of the world oceans. Note that ζ_g and ω_{min}/f were estimated from the monthly mean CMEMS reanalysis data of December 2013 as same as the KEx above. The depth was chosen between a depth that was 20 m deeper than the MLD (to avoid the non-geostrophic high shear zone below the ML, e.g. Figure 7b) and -1062m. When $|Ro_g| > 1,\ 1 + Ro_g - Ri_g^{-1} < 0$, or $Ri_g^{-1} > 4,\ \omega_{min}/f$ was not used.

Accepted for publication in *Journal of Physical Oceanography*. DOI 10.1175/JPO-D-20-0281.1.

5. Conclusion and Discussion

The role of near-inertial wind energies, which dissipate locally below the surface ML, on the climate system is studied by adopting the parameterization developed by Jochum et al. (2013) to a coarse-forward OGCM forced by assimilated forcing fields (ESTOC; Osafune et al. 2015) and integrating it for 58 years with the six-hourly wind data of the NCEP/NCAR reanalysis (Kalnay et al. 1996). We compared the parameterization with an EM-APEX float observation. Our conclusions are summarized as follows:

- The OGCM reproduces the near-inertial oscillations in the ML after storms as well as subsequent radiations of the near-inertial internal waves. The near-inertial waves radiating from the ML are low-mode internal waves whose meridional wavenumbers are influenced by the beta effect.

- The ratio, $\alpha^* = \int \frac{\partial KE_{ML}}{\partial t} dt / \int \boldsymbol{\tau} \cdot \boldsymbol{U_i}\, dt$, in the ML was examined with the OGCM. The wind energy input to the world ocean, $\int \boldsymbol{\tau} \cdot \boldsymbol{U_i}\, dA$, in January 1957 is 0.22 TW and the monthly average global $\int E^{flux}\, dA$ estimated from the last term of Eq. (3) with $\alpha^* = 0.2$ in January 1957 is 0.26 TW. Both exclude the equatorial region (5°N-5°S).

- Above estimated E^{flux} was used to diagnose the vertical diffusivities due to near-field wind mixing, which enhances the diffusivities below the ML. A comparison between four cases (CTRL, HFW-nJ, HFW-J, and HFW-Jh as explained in Section 2) in the final year suggests that the high-frequency winds cause warming above the main thermocline. The parameterized diffusivities, k_{niw}, increase around the equator, and it is consistent with Jochum et al. (2013). Since the east low–west

Accepted for publication in *Journal of Physical Oceanography*. DOI 10.1175/JPO-D-20-0281.1.

high SST contrast in the Pacific and Atlantic Oceans in the HFW-Jh case can be caused by an adjustment to the vertical mixing around the equator, the better understanding of near-inertial motions in the equatorial region is required.

- We investigated the possible effects of near-field wind mixing due to storm track activities in the North Pacific, which are modulated by the Aleutian low on the decadal scale. We applied the parameterization, excluding 20°N–20°S, to isolate effects of the Aleutian low. The regression coefficient to the PDO index decreases and increases in the shallower and deeper depths, respectively, at the center of the PDO. Thus, vertical water exchange by vertical mixing transfers the PDO signal into the deeper layer.
- Due to the possible importance of near-field wind mixing on the climate system, we evaluated the parameterization by the EM-APEX observation. The EM-APEX float observed an abrupt and local propagation of the near-inertial internal waves within NPSTMW and shear instabilities in the layer between the NPSTMW and NPIW in the KEx for 460 km along its trajectory. Even after considering the WKB stretching, the vertical diffusivities inferred from the parameterization do not reproduce the enhanced diffusivities in the deeper layer inferred from EM-APEX float measurements. Ray tracing of near-inertial waves near the KEx indicates that these instabilities are caused by wave trapping where low-mode energies are also dissipated. Therefore, vertical diffusivities due to trapping of the near fronts need to be parameterized separately.

Previous studies have concluded that near-inertial internal wave energies are not important for driving abyssal mixing because low-mode wave energies, which can reach

Accepted for publication in *Journal of Physical Oceanography*. DOI 10.1175/JPO-D-20-0281.1.

the main thermocline, are small. However, this study shows that wave energies can change the subsurface temperature fields and that the effects are modulated according to storm tracks, possibly on decadal time scales. Additionally, the trapping of near-inertial waves enhances local mixing in the main thermocline. Hence, the near-inertial waves should be treated separately in the parameterization because this trapping process dissipates low-mode wave energies (e.g., Kunze 1985). Consequently, a new parameterization for the trapping near fronts needs to be developed. We also note that it is possible to increase the kinetic energy of waves through an interaction with a mean flow (e.g., Lee and Niiler 1998). Finally, since the EM-APEX float did not measure turbulence directly, testing the parameterization by Jochum et al. (2013) using in situ microstructure measurements should be investigated in the future. We also speculate that, as stated by Jochum et al. (2013), understanding near-inertial motions near the equator is important to better understand the climate system.

Acknowledgements

We are indebted to Dr. Tadashi Hemmi for helping the numerical simulation and to Dr. Takeyoshi Nagai for deploying the EM-APEX during the KH-15-4 cruise. This study was supported by a Grant-in-Aid for Scientific Research on Innovative Areas (MEXT KAKENHI-JP15H05817, JP15H05818 and JP15H05819). A part of this study has been conducted using E.U. Copernicus Marine Service Information.

Accepted for publication in *Journal of Physical Oceanography*. DOI 10.1175/JPO-D-20-0281.1.

Appendix A. Ray path of near-inertial internal waves

The intrinsic frequency of near-inertial waves near ocean fronts is defined as (Kunze, 1985)

$$\omega \approx f_{eff} + \frac{N^2 k_H^2}{2fm^2} + \frac{1}{m}\left(\frac{\partial u_g}{\partial z} l - \frac{\partial v_g}{\partial z} k\right) \qquad (A1).$$

Here, $f_{eff} \approx f + \zeta_g/2$, $\zeta_g = \partial v_g/\partial x - \partial u_g/\partial y$, and $k_H^2 = k^2 + l^2$, where k, l, and m are the zonal, meridional, and vertical wavenumbers, respectively. Trapping of inertial waves occurs when ω is equal to the minimum frequency, which is defined by Whitt and Thomas (2013) as

$$\omega_{min} = f\sqrt{1 + Ro_g - Ri_g^{-1}} \approx f\left(1 + \frac{Ro_g - Ri_g^{-1}}{2}\right) \qquad (A2).$$

Here, $Ro_g = \zeta_g/f$, $Ri_g = N^2/\left[\left(\partial u_g/\partial z\right)^2 + \left(\partial v_g/\partial z\right)^2\right]$ and $-1 < Ro_g - Ri_g^{-1} \ll 1$. (A1) becomes (A2) when the oscillations are along a constant buoyancy surface. Using the intrinsic frequency $(A1)$, the group velocities can be written as

$$C_g^x = \frac{\partial \omega}{\partial k} \approx \frac{N^2 k}{fm^2} - \frac{1}{m}\frac{\partial v_g}{\partial z} \qquad (A3),$$

$$C_g^y = \frac{\partial \omega}{\partial l} \approx \frac{N^2 l}{fm^2} + \frac{1}{m}\frac{\partial u_g}{\partial z} \qquad (A4),$$

$$C_g^z = \frac{\partial \omega}{\partial m} \approx -\frac{N^2 k_H^2}{fm^3} - \frac{1}{m^2}\left(\frac{\partial u_g}{\partial z} l - \frac{\partial v_g}{\partial z} k\right) \qquad (A5).$$

The ray equations are consistent with equations of the wavenumbers,

$$\frac{d\boldsymbol{k}}{dt} = -\nabla\omega_E \qquad (A6),$$

where $\boldsymbol{k} = (k, l, m)$, $\nabla = (\partial/\partial x, \partial/\partial y, \partial/\partial z)$, and ω_E is the Euler frequency, and wave positions,

Accepted for publication in *Journal of Physical Oceanography*. DOI 10.1175/JPO-D-20-0281.1.

$$\frac{dx}{dt} = \frac{\partial\omega}{\partial k} + u_g = C_g^x + u_g \qquad (A7),$$

$$\frac{dy}{dt} = \frac{\partial\omega}{\partial l} + v_g = C_g^y + v_g \qquad (A8),$$

$$\frac{dz}{dt} = \frac{\partial\omega}{\partial m} = C_g^z \qquad (A9).$$

To solve the ray equations, we assume that the current is only in the zonal direction, the cross current section is in the meridional direction, and f is a constant. Since our goal is to demonstrate the possibility of inertial-wave trapping between NPSTMW and NPIW, we arbitrarily set the meridional wavelength to 50 km to numerically integrate the ray equation because this value corresponds to the width of the negative relative vorticity region and a vertical wavelength of 100 m. We also set a zonal wavelength to 0 to avoid a doppler shift.

References

Alford, M. H., 2001. Internal swell generation: The spatial distribution of energy flux from the wind to mixed layer near-inertial motions. J. Phys. Oceanogr., 31, 2359–2368.

Alford, M. H., 2003. Improved global maps and 54-year history of wind work on ocean inertial motions. Geophys. Res. Lett., 30, 1424.

Alford, M. H., and M. Whitmont, 2007. Seasonal and spatial variability of near-inertial kinetic energy from historical moored velocity records. J. Phys. Oceanogr., 37, 2022–2037.

Alford, M. H., J. A. MacKinnon, H. L. Simmons, and J. D. Nash, 2016. Near-inertial internal gravity waves in the ocean. Annual Review of Marine Science, 8, 95-123.

Accepted for publication in *Journal of Physical Oceanography*. DOI 10.1175/JPO-D-20-0281.1.

Crawford, G. B. and W. G. Large, 1996. A Numerical Investigation of Resonant Inertial Response of the Ocean to Wind Forcing. *J. Phys. Oceanogr.*, 26, 873–891.

D'Asaro, E. A., 1985. The energy flux from the wind to near inertial motions in the mixed layer. J. Phys. Oceanogr., 15, 1043–1059,

D'Asaro, E. A., C. C. Eriksen, M. A. Levine, P. Niiler, C. A. Paulson and P. van Meurs, 1995. Upper ocean inertial currents forced by a strong storm. Part I: Data and comparisons with linear theory. *J. Phys. Oceanogr.*, 25, 2909-2936.

Di Lorenzo, E., G. Liguori, N. Schneider, J. C. Furtado, B. T. Anderson, and M. A. Alexander, 2015. ENSO and meridional modes: A null hypothesis for Pacific climate variability. Geophys. Res. Lett., 42, 9440–9448.

Efron, B., and G. Gong, 1983. A leisurely look at the bootstrap, the jackknife and cross!validation. The American Statistician, 37, 36–48.

Furuichi N., T. Hibiya, and Y. Niwa, 2008. Model predicted distribution of wind-induced internal wave energy in the world's oceans. J. Geophys. Res., 113:C09034

Gargett, A. E. 1984. Vertical eddy diffusivity in the ocean interior, J. Mar. Res., 42, 359–393, doi:10.1357/002224084788502756.

Gent, P. R., and J. C. McWilliams 1990. Isopycnal mixing in ocean circulation models, J. Phys. Oceanogr., 20(1), 150–155.

Gill, A. E. 1984. On the behavior of internal waves in the wake of a storm. *J. Phys. Oceanogr.*, 14, 1129-1151.

Hasumi, H., and N. Suginohara, 1999. Effects of locally enhanced vertical diffusivity over rough topography on the world ocean circulation, J. Geophys. Res., 104, 23,364–

Accepted for publication in *Journal of Physical Oceanography*. DOI 10.1175/JPO-D-20-0281.1.

23,374, doi:10.1029/1999JC099191.

Inoue, R., M. Watanabe, and S. Osafune, 2017. Wind-induced mixing in the North Pacific J. Phys. Oceanogr., 47, 1587-1603.

Jochum, M., B. P. Briegleb, G. Danabasoglu, W. G. Large, N. J. Norton, S. R. Jayne, M. H. Alford, and F. O. Bryan, 2013. The impact of oceanic near-inertial waves on climate. J. Climate, 26, 2833-2844.

Kalnay, E., and Coauthors, 1996. The NCEP/NCAR 40-year reanalysis project. Bull. Amer. Meteor. Soc., 77, 437–471.

Kunze, E. 1985. Near-inertial wave propagation in geostrophic shear, J. Phys. Oceanogr., 14, 544-565.

Kunze, E., A. J. Williams, and M. G. Briscoe, 1990. Observations of shear and vertical stability from a neutrally-buoyant float. J. Geophys. Res., 95, 18127–18142.

Lee, D., and P. P. Niiler, 1998. The inertial chimney: the near-inertial energy drainage from the ocean surface to the deep layer. J. Geophys. Res., 103, 7579-7591.

Mantua, N. J., S. R. Hare, Y. Zhang, J. M. Wallace, and R. Francis, 1997. A Pacific interdecadal climate oscillation with impacts on salmon production. Bull. Amer. Meteor. Soc., 78, 1069-1079.

Munk, W. H., 1966. Abyssal recipes. Deep-Sea Res. Oceanogr. Abstr., 13, 707–730.

Munk, W. H., and C. Wunsch, 1998. Abyssal recipes II: Energetics of tidal and wind mixing. Deep-Sea Res. I, 45, 1977-2010.

Nagasawa, M., Y. Niwa, and T. Hibiya, 2000. Spatial and temporal distribution of the wind-induced internal wave energy available for deep water mixing in the North

Accepted for publication in *Journal of Physical Oceanography*. DOI 10.1175/JPO-D-20-0281.1.

Pacific. J. Geophys. Res., 105, 13933-13943.

Noh, Y. 2004. Sensitivity to wave breaking and the Prandtl number in the ocean mixed layer model and its dependence on latitude, Geophys. Res. Lett., 31, L23305, doi:10.1029/2004GL021289.

Osafune, S., T. Doi, S. Masuda, N. Sugiura, and T. Hemmi, 2014. Estimated state of ocean for climate research (ESTOC). JAMSTEC. doi:10.17596/0000106 (accessed 2019-05-14).

Osafune, S., S. Masuda, N. Sugiura, and T. Doi, 2015. Evaluation of the applicability of the Estimated State of the Global Ocean for Climate Research (ESTOC) data set, Geophys. Res. Lett., 42, doi:10.1002/2015GL064538.

Osafune, S., Kouketsu, S., Masuda, S., & Sugiura, N. 2020. Dynamical ocean response controlling the eastward movement of a heat content anomaly caused by the 18.6-year modulation of localized tidally induced mixing. J. Geophys. Res., *125*, e2019JC015513. https://doi.org/10. 1029/2019JC015513

Pacanowski, R., and S. Griffies, 2000. MOM 3.0 Manual, 680 pp., Geophys. Fluid Dyn. Lab., Princeton, N. J.

Pollard, R. T. and R. C. Millard, 1970. Comparison between observed and simulated wind-generated inertial oscillations. *Deep-Sea Res.*, 17, 153-175.

Rimac, A., J.-S. von Storch, C. Eden, and H. Haak, 2013. The influence of high-resolution wind stress fields on the power input to near-inertial motions in the ocean. *Geophys. Res. Lett.*, 40, 4882–4886.

Sanford, T. B., J. H. Dunlap, J. A. Carlson, D. C. Webb, and J. B.Girton, 2005.

Accepted for publication in *Journal of Physical Oceanography*. DOI 10.1175/JPO-D-20-0281.1.

Autonomous velocity and density profiler: EM-APEX. Proc. Eighth Working Conf. on Current Measurement Technology, Southampton, United Kingdom, IEEE/OES, 152–156.

Sugimoto, S., and K. Hanawa, 2009. Decadal and interdecadal variations of the Aleutian Low activity and their relation to upper oceanic variations over the North Pacific. J. Meteor. Soc. Japan, 87, 601–614.

Tsujino, H., H. Hasumi, and N. Suginohara, 2000. Deep Pacific circulation controlled by vertical diffusivity at the lower thermocline depths, J. Phys. Oceanogr., 30, 2853–2865, doi:10.1175/1520-0485(2001)031, 2853–2865.

Watanabe, M., and T. Hibiya, 2002. Global estimates of the wind-induced energy flux to inertial motions in the surface mixed layer. Geophys. Res. Lett., 29, 1239, doi:10.1029/2001GL04422.

Whalen, C. B., L. D. Talley, and J. A. MacKinnon, 2012. Spatial and temporal variability of global ocean mixing inferred from Argo profiles. Geophys. Res. Lett., 39, L18612, doi:10.1029/2012GL053196.

Whitt, D. B. and L. N. Thomas, 2013. Near-inertial waves in strongly baroclinic currents, J. Phys. Oceanogr., 43, 706-725.

Zhai, X., R. J. Greatbatch, C. Eden, and T. Hibiya, 2009. On the loss of wind-induced near-inertial energy to turbulent mixing in the upper ocean. *J. Phys. Oceanogr.*, 39, 3040-3045.

Accepted for publication in *Journal of Physical Oceanography*. DOI 10.1175/JPO-D-20-0281.1.

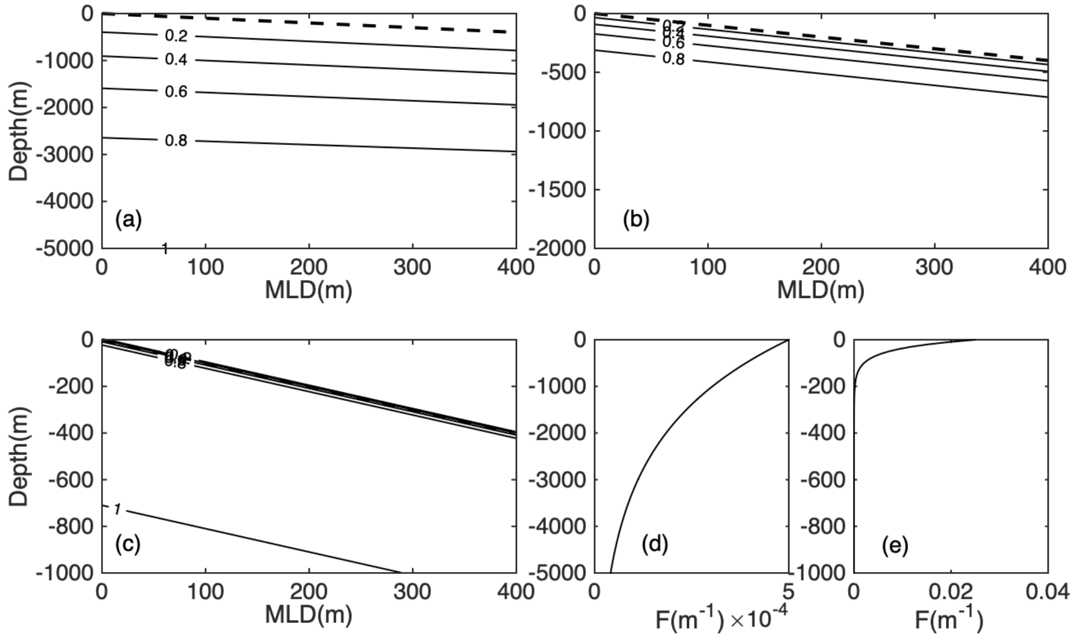

Figure 1. Vertically integrated structure functions for (a) η = 2000 m, (b) η = 200 m, and (c) η = 20 m as functions of the ML depth (the thick dashed line, $-h$). The integration is started from the ML depth to each depth. Structure function F with (d) η = 2000 m and (e) η = 40 m. Bottom depth $-H$ = −5000 m is used in the calculation.

Accepted for publication in *Journal of Physical Oceanography*. DOI 10.1175/JPO-D-20-0281.1.

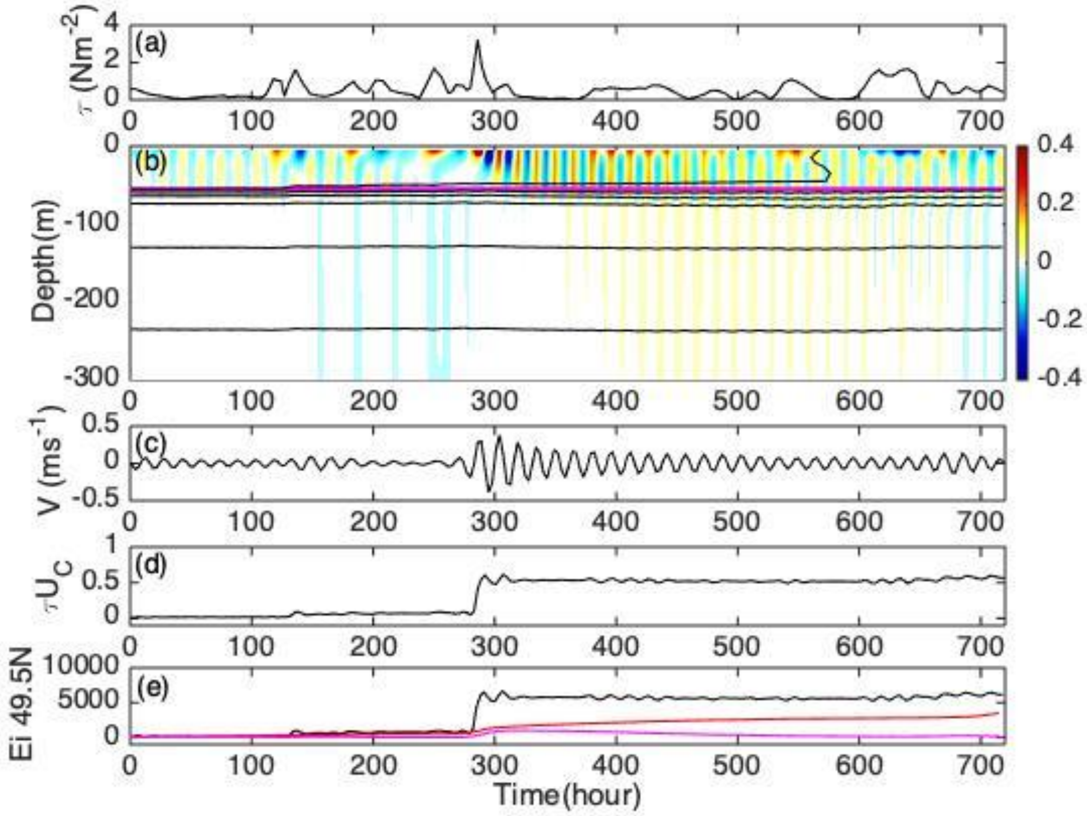

Figure 2. Time series of (a) wind stress, $|\tau| = \left(\tau_x^2 + \tau_y^2\right)^{\mathbf{1/2}}$, (b) meridional velocity (m s^{-1}), (c) surface meridional velocity of near-inertial currents, (d) Cumulative value of $\boldsymbol{\tau} \cdot \boldsymbol{U_i}$, $\tau \cdot U_C = \sum_{t=0} \boldsymbol{\tau} \cdot \boldsymbol{U_i}$, and (e) KE_{ML} (magenta line), $\int \boldsymbol{\tau} \cdot \boldsymbol{U_i}\, dt$ (black), and $\int E^{flux}\, dt$ (red) at 174.5°E and 49.5°N. x-Axis indicates the elapsed time from the start of the numerical simulation, 1957/1/1. Contour lines in (b) are σ_θ with a contour interval of 0.1 kg m^{-3}.

Accepted for publication in *Journal of Physical Oceanography*. DOI 10.1175/JPO-D-20-0281.1.

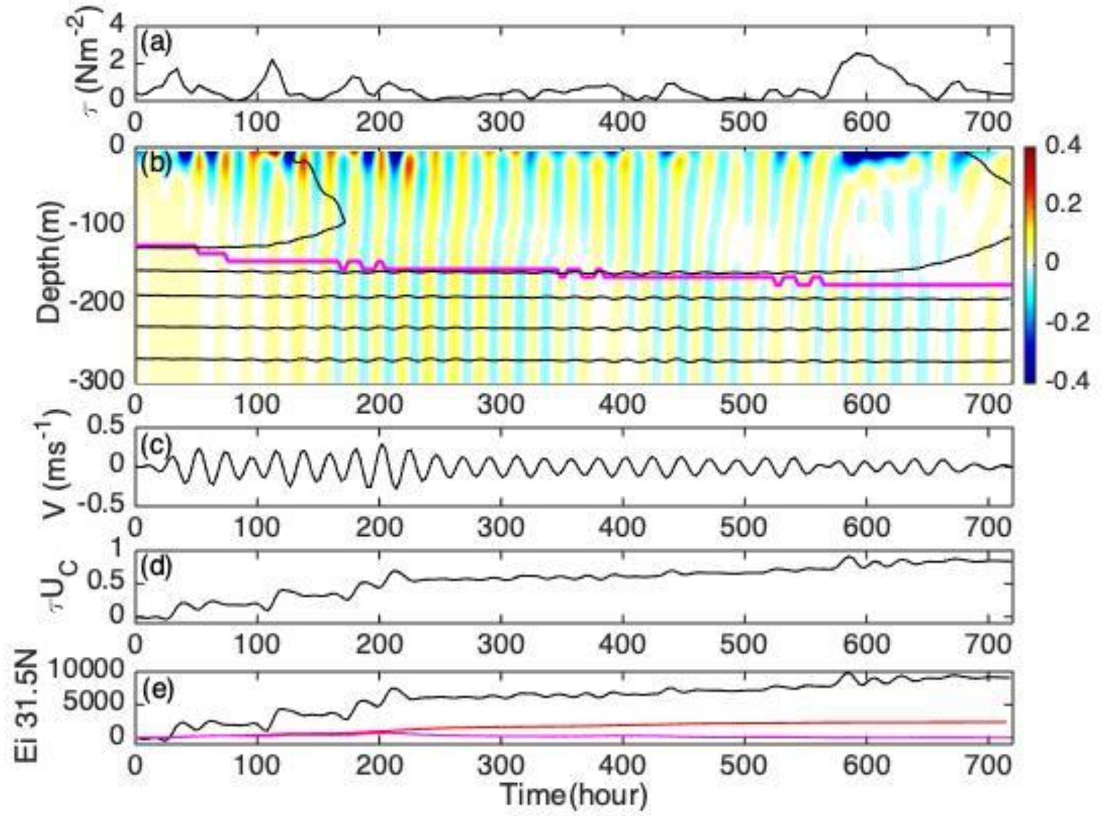

Figure 3. Same as Fig. 2 but for 31.5°N.

Accepted for publication in *Journal of Physical Oceanography*. DOI 10.1175/JPO-D-20-0281.1.

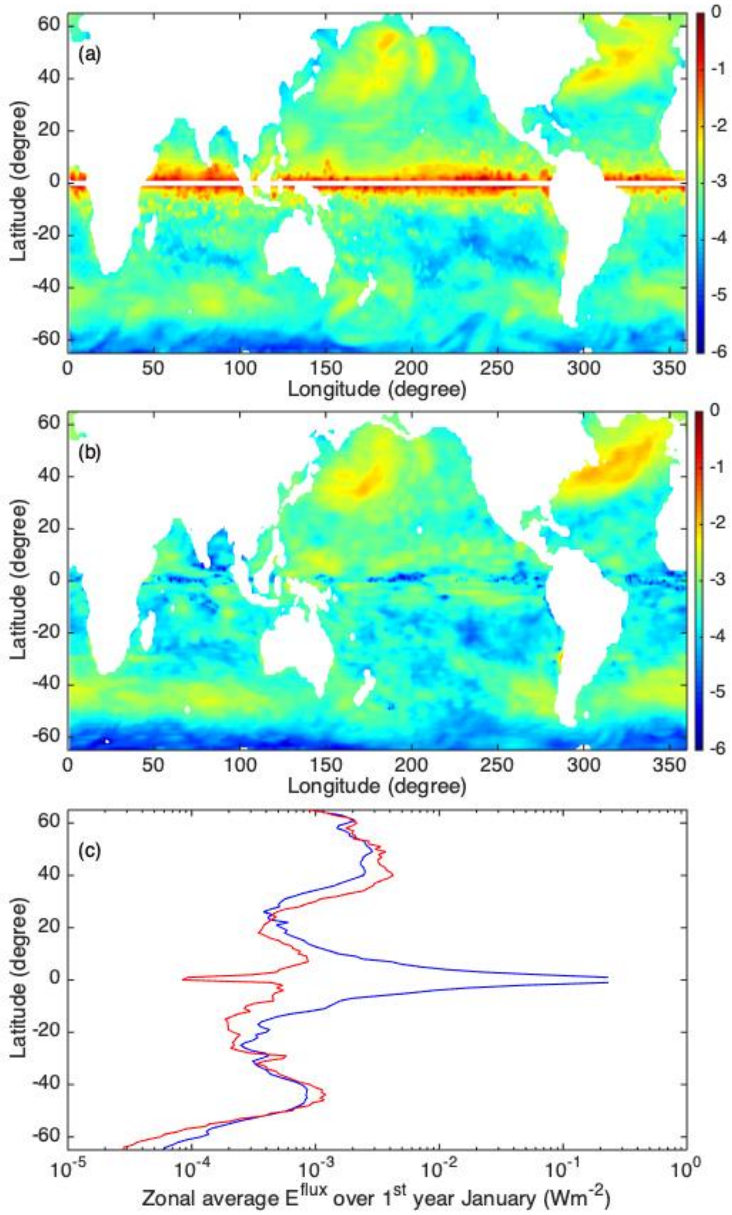

Figure 4. Horizontal distributions of (a) E^{flux} in the HFW-Jh estimated by Eq. (3) and (b) $\boldsymbol{\tau} \cdot \boldsymbol{U_i}$ in the HFW-nJ estimated by the band-passed surface velocities for every three hours. The $\log_{10}$ of magnitudes are shown. (c) Zonal average of the E^{flux} (blue line) and that of $\boldsymbol{\tau} \cdot \boldsymbol{U_i}$ (red line).

Accepted for publication in *Journal of Physical Oceanography*. DOI 10.1175/JPO-D-20-0281.1.

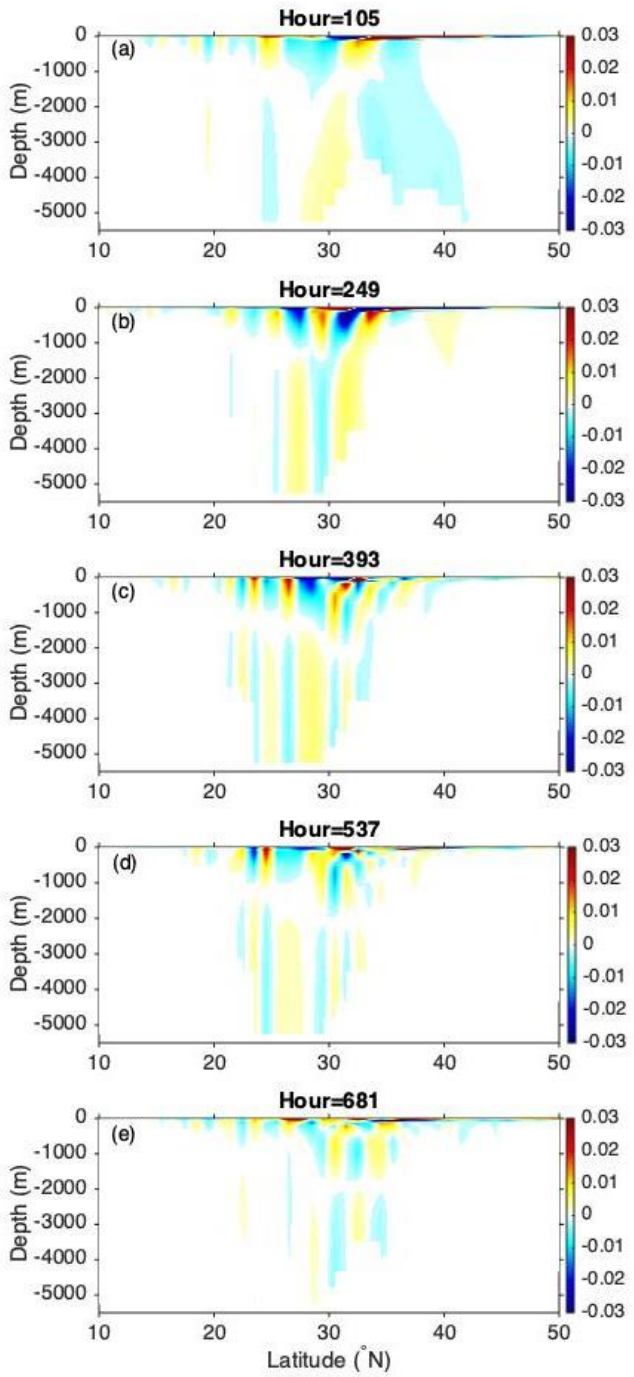

Figure 5. Vertical cross-sections of (a–e) meridional velocity fields and (f–j) bandpass-filtered (between Coriolis frequencies of 30°N and 35°N) meridional velocities every 6 days along 174.5°E. Hours at the top of each panel denote the elapsed time from the start of the numerical simulation.

Accepted for publication in *Journal of Physical Oceanography*. DOI 10.1175/JPO-D-20-0281.1.

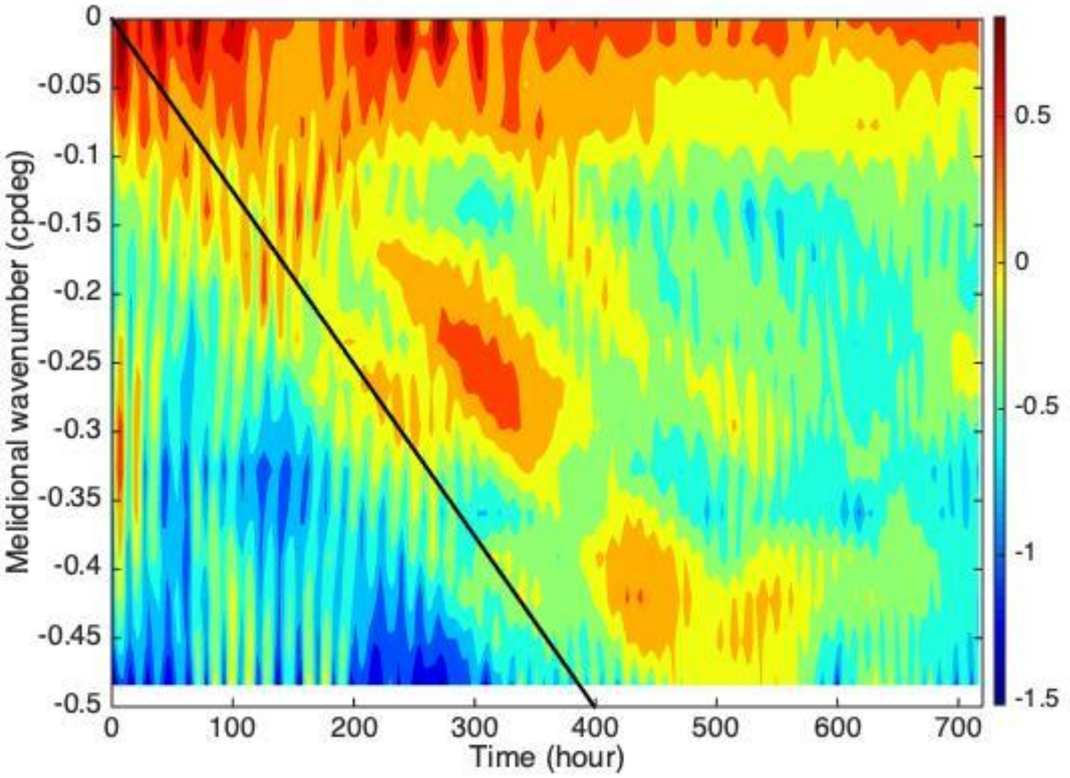

Figure 6. Time series of the $\log_{10}$ values of the variances of meridional velocities in 9.5–40.5°N and 143.5°E–179.5°W. Black line shows the wavenumber of $-df/dy \times Time$ at 30.5°N. Geographical coordinate is used to calculate spectra. x-Axis indicates the elapsed time from the start of the numerical simulation.

Accepted for publication in *Journal of Physical Oceanography*. DOI 10.1175/JPO-D-20-0281.1.

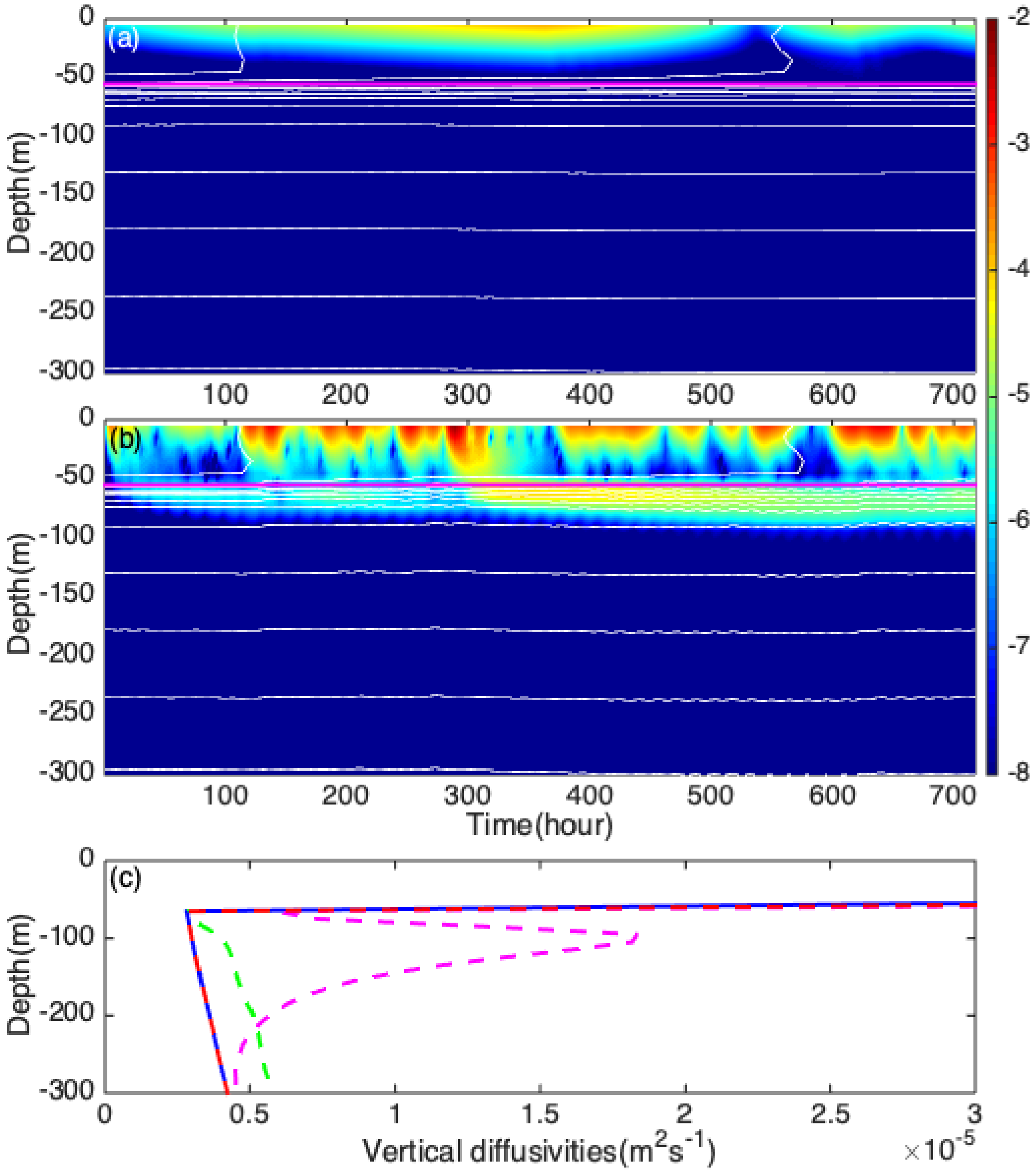

Figure 7. Time series of (a) $\log_{10}$ of shear squared (sec^{-2}) from the CTL and (b) the HFW-J. Contour lines are σ_θ with a contour interval of 0.1 kg m^{-3}. Magenta line is the ML base. x-Axis is the elapsed time from the start of the numerical simulation. Vertical profiles of (c) the monthly average total diffusivities used to calculate temperature fields, k_T, from the CTL (blue), HFW-nJ (red dashed), HFW-J (green dashed), and HFW-Jh (magenta dashed) at 174.5°E and 49.5°N.

Accepted for publication in *Journal of Physical Oceanography*. DOI 10.1175/JPO-D-20-0281.1.

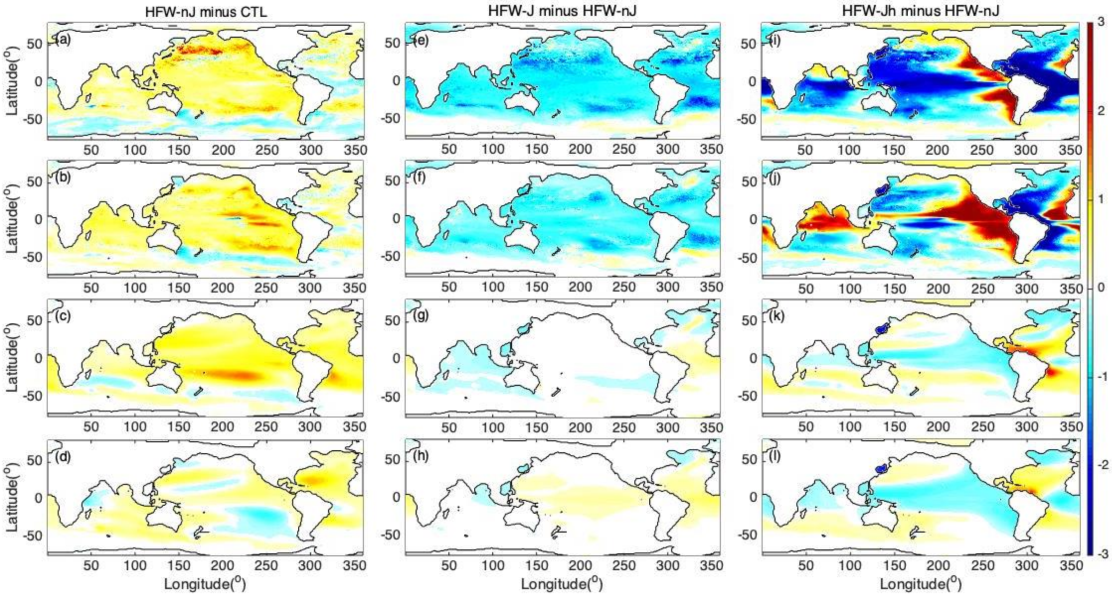

Figure 8. Horizontal distributions of the differences between yearly average (final 58th year, 2014) temperatures (HFW-nJ minus CTL), at (a) -5 m, (b) -105 m, (c) -477 m, and (d) -719 m. Those of HFW-J minus HFW-nJ at (e) -5 m, (f) -105 m, (g) -477 m, and (h) -719 m. Those of HFW-Jh minus HFW-nJ, at (i) -5 m, (j) -105 m, (k) -477 m, and (l) -719 m.

Accepted for publication in *Journal of Physical Oceanography*. DOI 10.1175/JPO-D-20-0281.1.

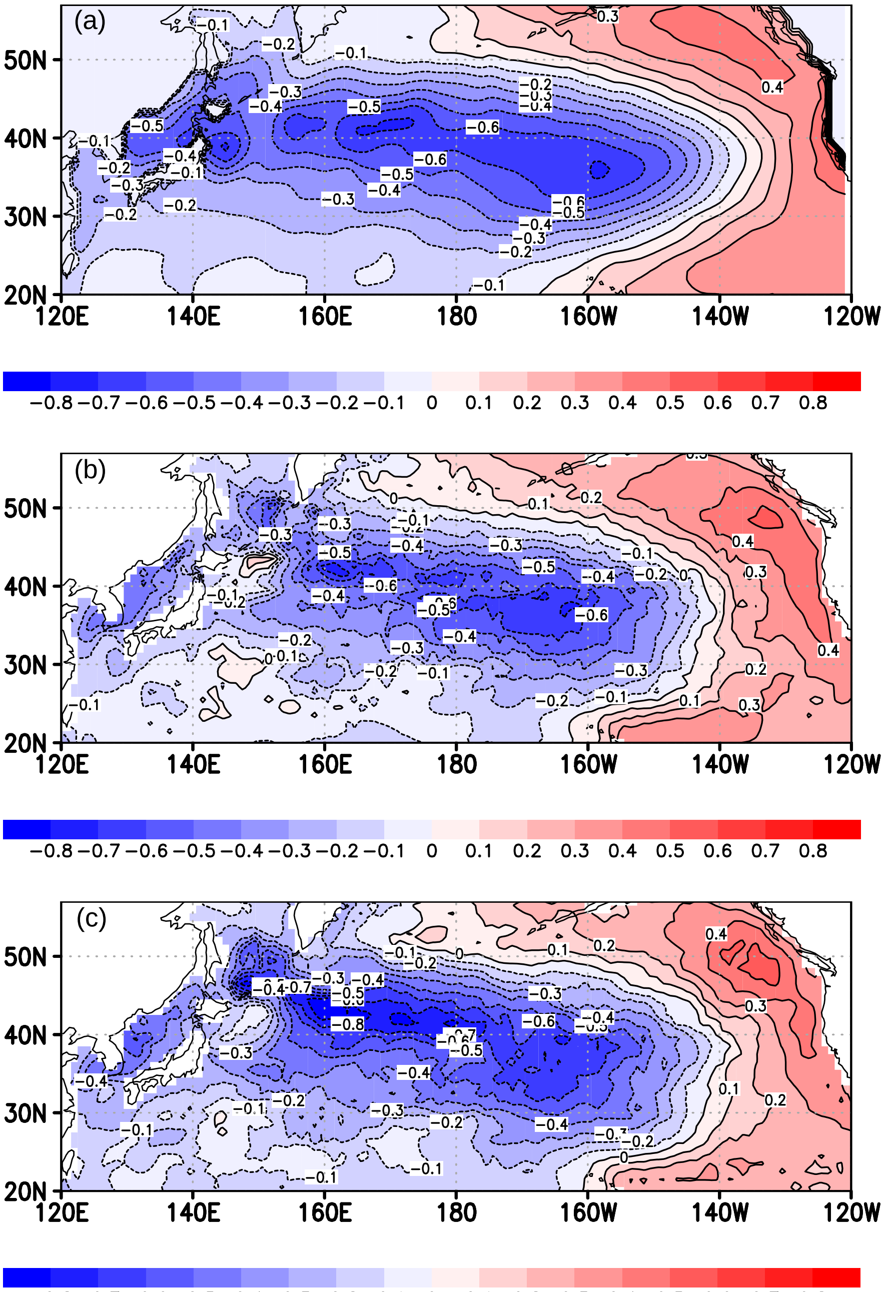

Figure 9. Horizontal distributions of (a) the EOF first mode of the observation and the regression coefficient between the PDO index and SST from (b) CTL and (c) HFW-nJ in the North Pacific.

Accepted for publication in *Journal of Physical Oceanography*. DOI 10.1175/JPO-D-20-0281.1.

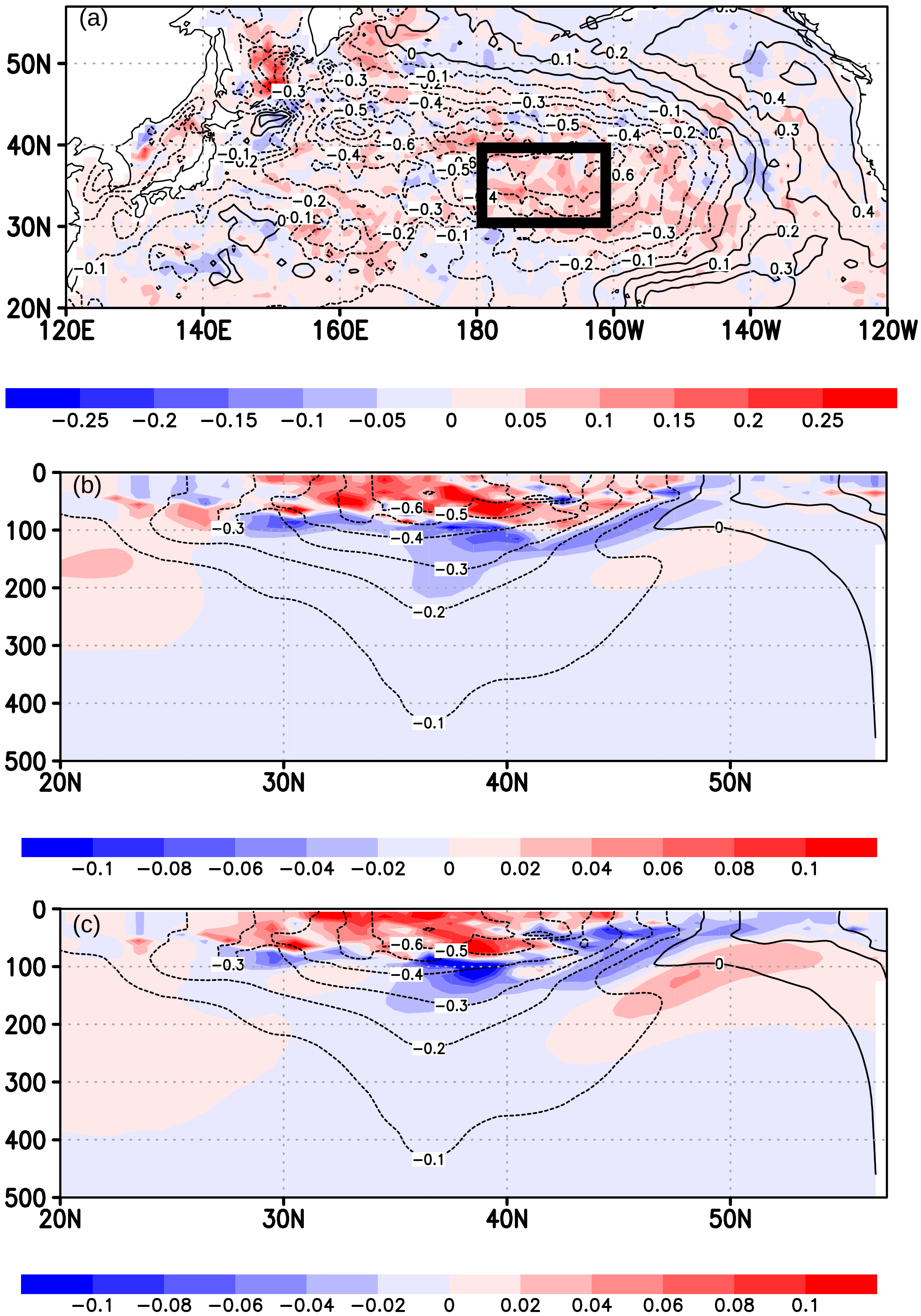

Figure 10. (a) Horizontal distributions of the regression coefficient from CTL (black line) and the differences of the coefficients between the HFW cases (HFW-J minus HFW-nJ, colored area). Vertical cross-section along 170°W for the (b) HFW-J and (c) HFW-Jh. Black line and colored area are the same as (a).

Accepted for publication in *Journal of Physical Oceanography*. DOI 10.1175/JPO-D-20-0281.1.

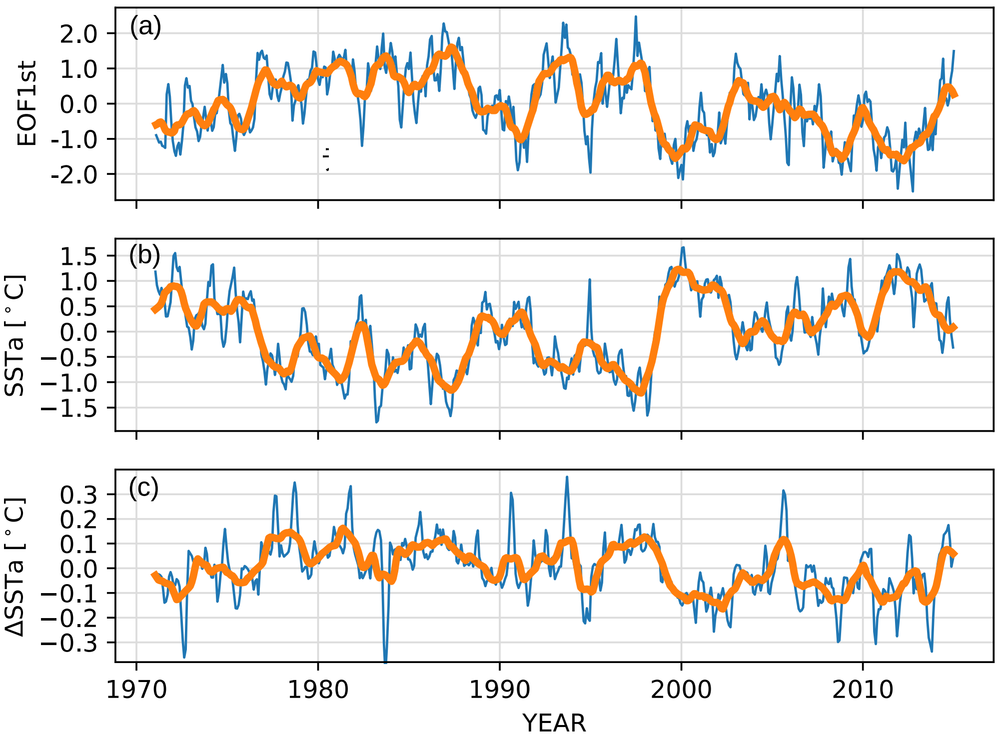

Figure 11. (a) PDO index, and time series of (b) the SST anomaly from CTL averaged over the black box in Figure 10(a) where the composite monthly mean is subtracted, and (c) differences of the average SST anomaly between the HFW cases (HFW-J minus HFW-nJ). Blue lines in (a)–(c) show the monthly means, and thick orange lines are the 13-month running mean.

Accepted for publication in *Journal of Physical Oceanography*. DOI 10.1175/JPO-D-20-0281.1.

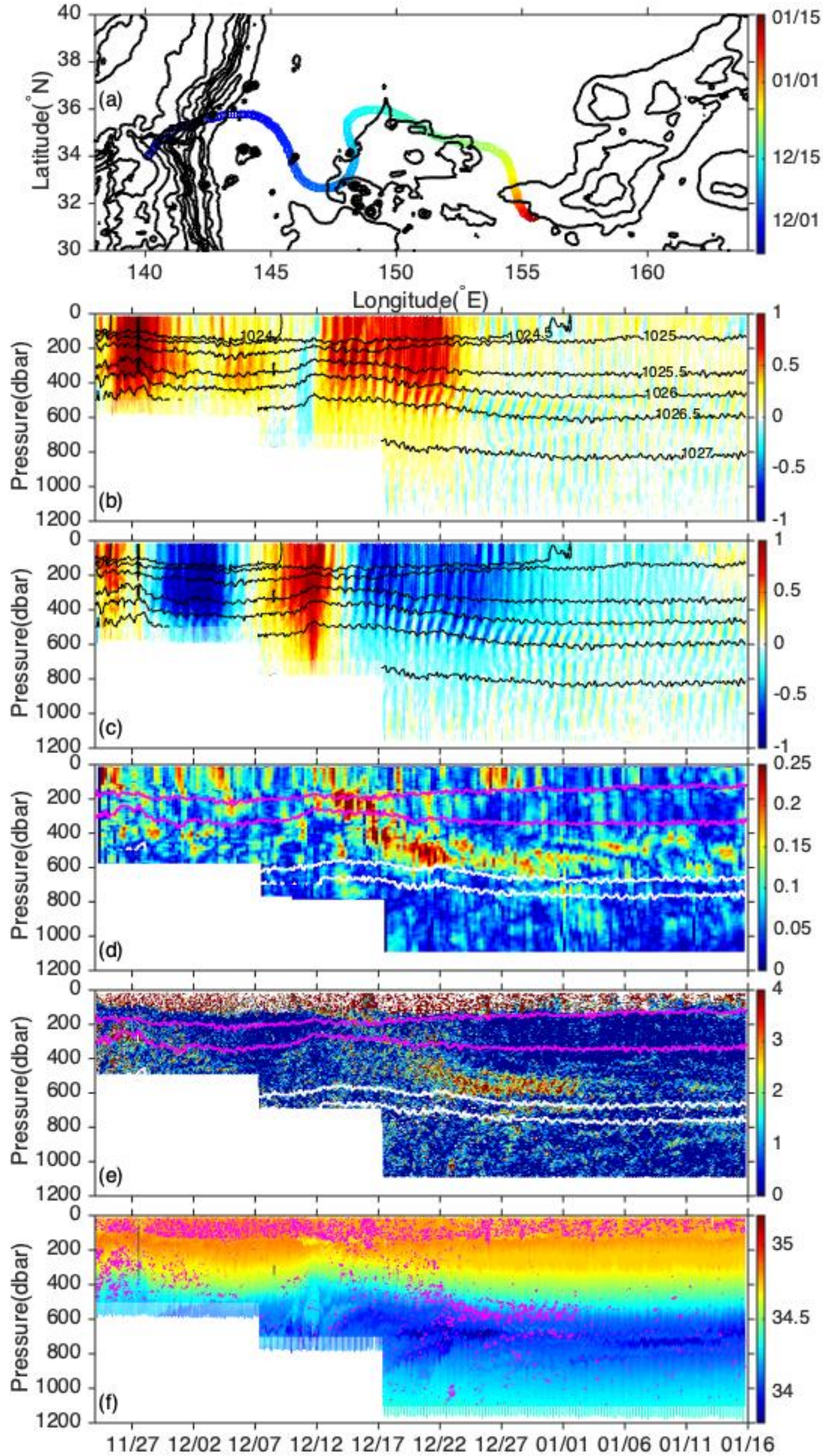

783

Accepted for publication in *Journal of Physical Oceanography*. DOI 10.1175/JPO-D-20-0281.1.

Figure 12. (a) Trajectory of the EM-APEX with the bottom topography. Color bar indicates the date in 2013. Time series of (b) zonal velocity, (c) meridional velocity, (d) high-passed (at 1cpd) near-inertial speed, $(U_i^2 + V_i^2)^{1/2}$, (e) inversed Ri, and (f) salinity. x-Axis is the date in 2013. Contour lines in (b–c) are the potential densities. Magenta lines in (d) and (e) are isotherms of 17 and 19°C, indicating the NPSTMW. White lines in (d) and (e) are potential densities of 1026.7 and 1026.9 kgm^{-3}, indicating the NPIW. Magenta line in (f) indicates that Ri is less than 1/4.

Accepted for publication in *Journal of Physical Oceanography*. DOI 10.1175/JPO-D-20-0281.1.

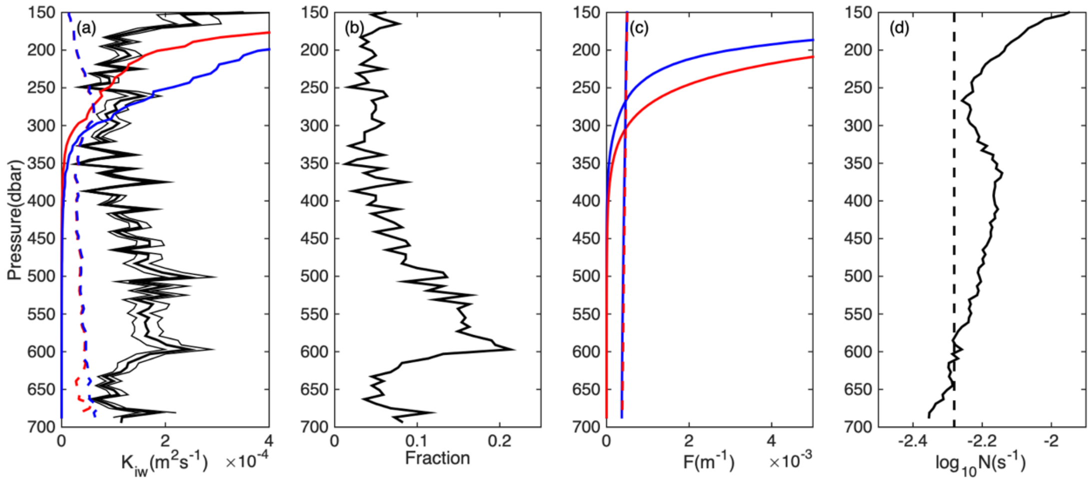

Figure 13. Vertical profiles of (a) the vertical diffusivities estimated from the EM-APEX float data with Eq. (11) (black line) from (1) (blue line), and from Eq. (1) with Eq. (12) (red line), (b) fraction of shear instability during a storm event, (c) distribution function from Eq. (8) (blue line) and Eq. (12) (red line), and (d) $\log_{10}$ value of the buoyancy frequency from the EM-APEX float (black line) and $N_0 = 3$ cph (black dashed line). In (a) and (c), WKB depth is estimated on the pressure coordinate, and the dashed line for η = 2000 m and solid line for η = 20 m. In (a), the 95 % confidence limit for the diffusivities estimated from the EM-APEX float data (black thin line) is obtained by the bootstrapping method (Efron and Gong 1983). Here, we assume that velocity measurements include random noises and the bootstrap is applied on $\langle \varepsilon \rangle$ in Eq. (8) at each layer which has same sample number.

Accepted for publication in *Journal of Physical Oceanography*. DOI 10.1175/JPO-D-20-0281.1.

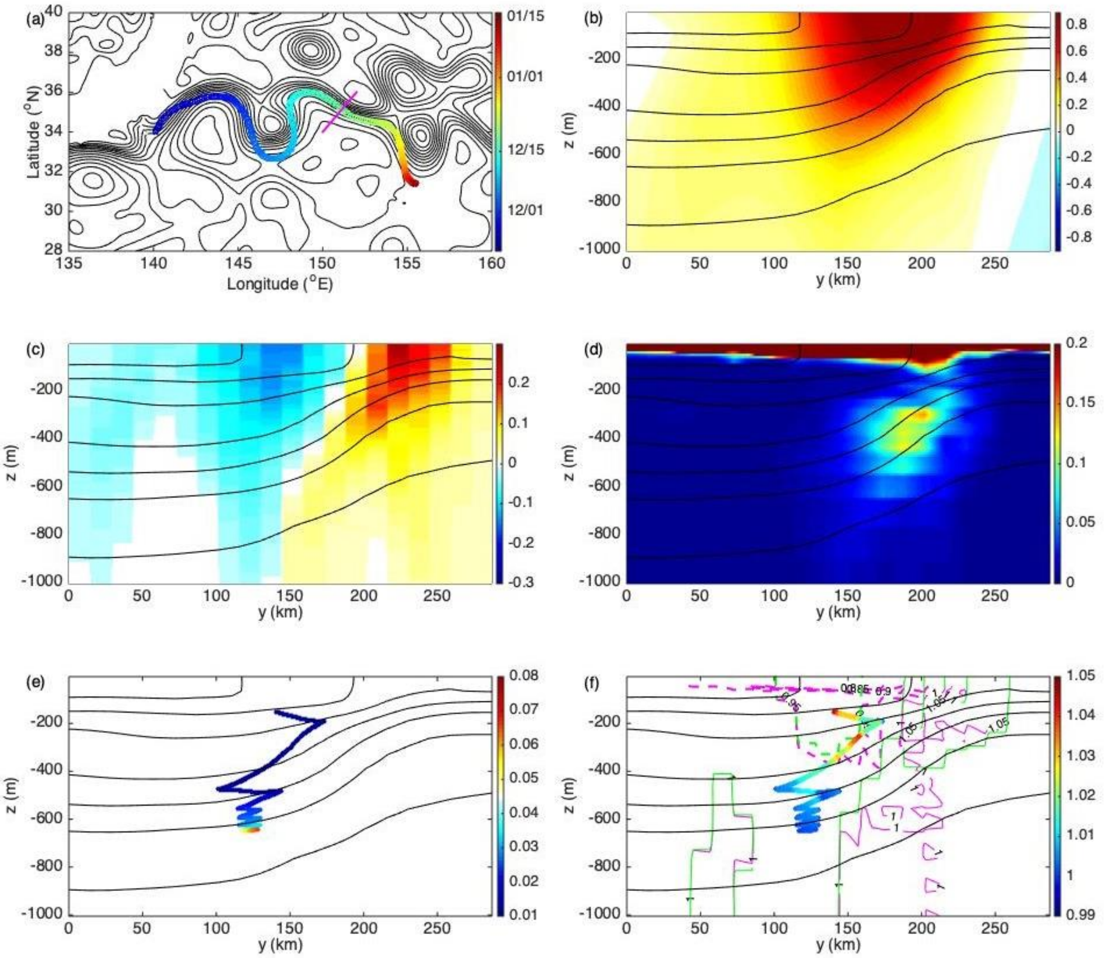

Figure 14. (a) Trajectory of the EM-APEX float on the sea surface height of the CMEMS reanalysis data. Magenta line shows the cross-section used in this study. Color bar indicates the date in 2013. Vertical cross-section of the (b) monthly mean speed, $(U^2 + V^2)^{1/2}$, (c) vertical component of the relative vorticity normalized with the local Coriolis frequency estimated at the same depth, (d) Ri_g^{-1} calculated from the monthly mean fields, (e) vertical wavenumber of the near-inertial wave along the ray path, and (f) intrinsic frequency of the near-inertial wave normalized with ω_{min}. Green and magenta contours are $1 + \zeta_g/2$ and ω_{min}/f, respectively. y = 0 km corresponds to the southwest end of the cross-section in (a).

Accepted for publication in *Journal of Physical Oceanography*. DOI 10.1175/JPO-D-20-0281.1.

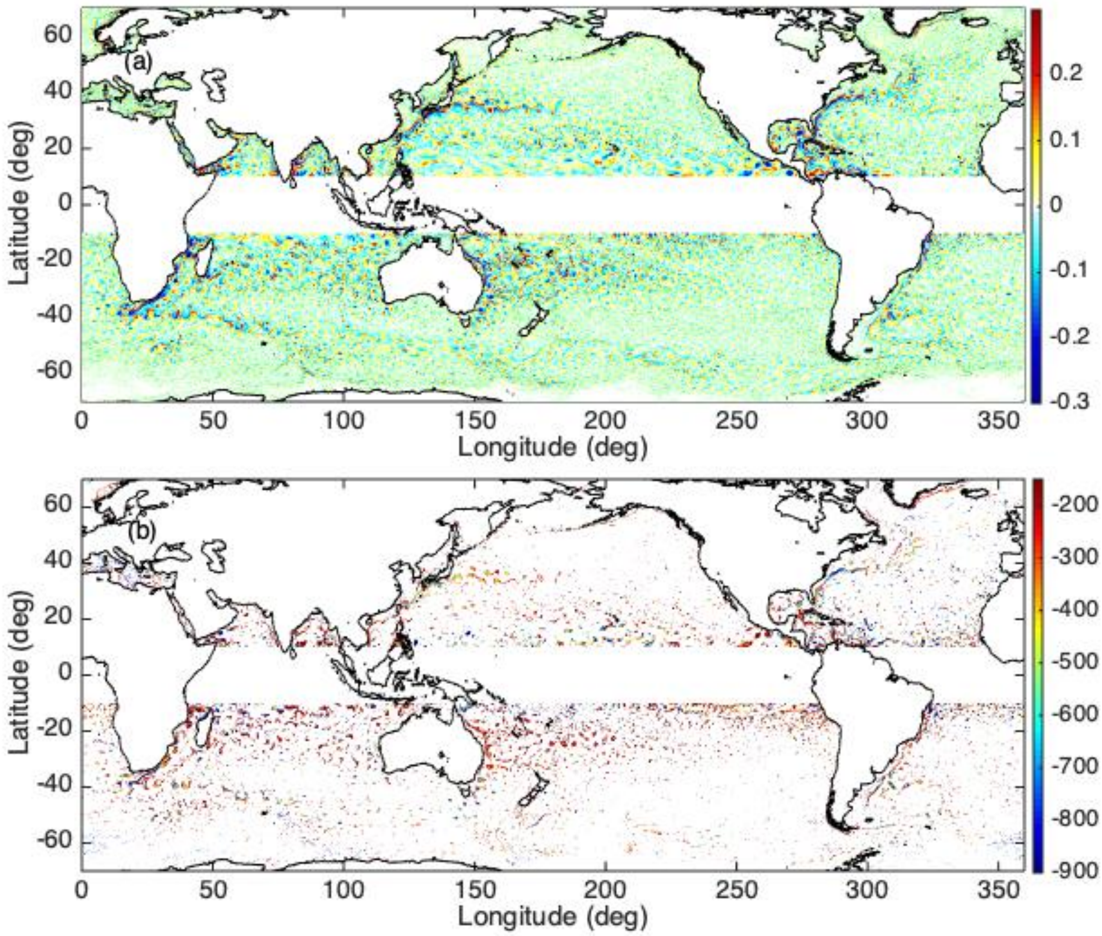

Figure 15. The horizontal distributions of (a) $Ro_g = \zeta_g/f$ at the sea surface (z = -0.5m) and (b) depth of the deepest layer where ω_{min}/f < 0.95 except for 10°N-10°S.

Accepted for publication in *Journal of Physical Oceanography*. DOI 10.1175/JPO-D-20-0281.1.